Research Square

Preprints are preliminary reports that have not undergone peer review.
They should not be considered conclusive, used to inform clinical practice,
or referenced by the media as validated information.

# Electro-oxidation of Polystyrene Nanoplastics Using a Titanium-based Anode Modified with Ag–Sn/Pb–$PbO_2$: ANN-PSO Modeling

**S. Mohammad Esmaeil Zakeri**
Shiraz University
**Mehrzad Feilizadeh**
m.feilizadeh@shirazu.ac.ir

Shiraz University

**Research Article**

**Keywords:** Electrooxidation, Polystyrene, Nanoplastics, Artificial neural network, Response surface methodology

**Posted Date:** November 4th, 2026

**DOI:** https://doi.org/10.21203/rs.3.rs-11224431/v1

**License:** This work is licensed under a Creative Commons Attribution 4.0 International License.
Read Full License

**Additional Declarations:** No competing interests reported.

# Electro-oxidation of Polystyrene Nanoplastics Using a Titanium-based Anode Modified with Ag–Sn/Pb–$PbO_2$: ANN-PSO Modeling

S. Mohammad Esmaeil Zakeri[1], Mehrzad Feilizadeh[1*]

*1. Department of Chemical Engineering, School of Chemical and Petroleum Engineering, Shiraz University, Shiraz, Iran*

**Abstract**

Polystyrene nanoplastics (PS NPs) are persistent water contaminants that conventional treatment processes struggle to remove. In this study, a multilayer Ti/$TiO_2$–Ag–Sn/Pb–$PbO_2$ (TASP) anode was synthesized and evaluated for the electro-oxidation of PS NPs. The TASP electrode exhibited a high oxygen-evolution potential of 1.97 V vs. Ag/AgCl, reduced charge-transfer resistance, and an extended accelerated service life of 188 s under harsh test conditions, indicating greater relative stability than the reference electrodes. The effects of pH, initial PS-NP concentration, and current density on removal efficiency were investigated using a maximin Latin hypercube design (LHS) augmented with a two-level factorial, and both RSM and ANN-PSO models were developed for process prediction. The ANN-PSO model showed superior predictive performance ($R^2$ = 0.953) compared with the RSM model ($R^2$ = 0.919), confirming its superior ability to capture the nonlinear behavior of the system. Coupling ANN-PSO with a genetic algorithm identified the optimum operating conditions to be pH 6.46, initial concentration 20 ppm, and current density 11.44 mA $cm^{-2}$, with a predicted removal efficiency of 90.64%. Experimental validation under the optimized conditions gave 91.43% removal within 90 min, confirming the reliability of the proposed optimization framework. Kinetic analysis showed that PS-NP degradation followed pseudo-first-order behavior, with the TASP electrode exhibiting the highest apparent rate constant, approximately 3.2 times greater than that of the unmodified Ti/$TiO_2$/Pb-$PbO_2$ electrode. These results demonstrate that combining an Ag–Sn-modified $PbO_2$-based anode and a data-driven modeling and optimization strategy provides an effective and interpretable approach for PS-NP electro-oxidation.

**Keywords:** Electrooxidation; Polystyrene; Nanoplastics; Artificial neural network; Response surface methodology

* Corresponding author, E-mail: m.feilizadeh@utwente.nl, m.feilizadeh@shirazu.ac.ir

## 1. Introduction

The widespread use of plastic products and their resistance to degradation have led to their accumulation in the environment [1]. These plastics are fragmented by organisms into microplastics (MPs, <5 mm) and nanoplastics (NPs, <1000 nm) [2-4]. Among the various types of NPs found in the environment, polystyrene (PS) is one of the most widely used plastics, with over 23 million tons produced annually [5]. PS is a key component of NPs and is used in various applications, including 3D printing in the textile industry to impart strength and flexibility [6]. Due to their harmful effects and the inefficiency of conventional water treatments in degrading NPs, effective technologies are needed to eliminate these pollutants from water sources [7].

Recent applications of advanced oxidation processes (AOPs), such as electrooxidation (EO) [8, 9] and Fenton-electrochemical oxidation [10], have shown promise in treating water pollution by generating highly reactive species such as $SO_4^{\bullet-}$, $^{\bullet}OH$, and $Cl^{\bullet}$. Among the different AOPs, EO is favored in water treatment due to its low cost, rapid processing, safety, and ease of operation [11, 12]. The efficiency of this process is significantly influenced by the choice of anodic material, which remains a key focus for many researchers.

When selecting anodic materials for EO of NPs, it is crucial to consider factors such as a high oxygen evolution potential (OEP) and the capacity to generate weakly adsorbed hydroxyl radicals [13, 14]. Taking these characteristics into account, a range of electrodes coated with metals and metal oxides exhibiting superior electrocatalytic activity have been systematically investigated for their efficacy in the EO process. The anode materials evaluated include β-$PbO_2$/Ti [15], Ti/$PbO_2$–$TiO_2$–$Ce(NO_3)_4$ [16], Ti/$PbO_2$ [17], $RuO_2$-$IrO_2$/Ti [18], Ti/α-$PbO_2$/β-$PbO_2$ [19], and $RuO_2$–PdO–$TiO_2$/Ti [20]. The Ti matrix offers significant advantages, including exceptional corrosion resistance, superior electrical conductivity, and a low overpotential for OEP [21]. However, its application is still largely restricted to laboratory research due to the high costs and limited operational lifespan associated with Ti [22, 23]. Moreover, while the $PbO_2$ electrode is widely recognized for its electrocatalytic performance, effective mineralization capabilities, and cost-efficiency [24, 25], it is not without drawbacks. Issues such as $Pb^{2+}$ leakage and suboptimal hydroxyl radical utilization highlight the need for further advances in electrode design [26].

To mitigate the issues associated with metal and metal oxide electrodes, researchers have explored doping the active layer with elements such as Sn, Ag, Sb, F, Ce, and La [27, 28]. This approach has enhanced degradation efficiency of NPs on the modified electrodes. Findings indicate that the

EO activity of these electrodes can be significantly improved by reducing the crystal size and increasing the OEP [29].

Incorporating an active layer such as Ag can decrease the current density, thereby mitigating corrosion and prolonging the anode's operational lifespan relative to pure anodes [30]. Furthermore, adding Sn as a sublayer can enhance the EO process by improving intrinsic electrocatalytic properties, elevating the OEP for more efficient generation of reactive oxygen species, and reinforcing the structural stability and electrical conductivity of the electrode [31, 32]. Examples of anode materials with active layers include $TiO_2$-NTs/Sb-$SnO_2$/$PbO_2$ [33], Ti/$SnO_2$–Sb/Co-β$PbO_2$ [12], Ti/$SnO_2$-$Sb_2O_4$-La/β-$PbO_2$ [34], Ti/Sn-$SbO_x$/β-$PbO_2$-$Ta_2O_5$ [35], Ti/$SnO_2$–Sb/La-β$PbO_2$ [36], and Ti/Sb-$SnO_2$/β-$PbO_2$ [37]. Thus, using Ti as the substrate, with Sn, Sb, and La as intermediate layers, and applying a $PbO_2$ coating can effectively leverage the benefits of each component.

Despite the growing use of Ti-based and $PbO_2$-based anodes in EO, most previous studies have focused on dissolved pollutants such as dyes, antibiotics, phenols, and ammonia, while limited attention has been paid to plastic pollutants, particularly PS NPs. In addition, many previously reported systems are based on conventional Ti/$PbO_2$, Ti/$TiO_2$/$PbO_2$, or single-modified $PbO_2$ architectures, whereas studies combining Ag and Sn simultaneously within a multilayer Ti/$TiO_2$-supported Pb/$PbO_2$ framework remain limited. Therefore, the present work is innovative in three main respects. First, it specifically addresses the electro-oxidative degradation of PS NPs, which are more challenging than dissolved contaminants because of their colloidal nature and interfacial behavior. Second, it develops a new Ti/$TiO_2$–Ag–Sn/Pb–$PbO_2$ (TASP) electrode that combines the conductivity-promoting role of Ag, the stability-enhancing effect of Sn, and the oxidation capability of $PbO_2$ in a single integrated architecture. Third, the material development is coupled with a process-analysis framework based on a maximin Latin hypercube design (LHS) augmented with a two-level factorial, comparative RSM and ANN-PSO modeling, GA-based optimization, and Garson sensitivity analysis. This enables not only efficient removal but also a predictive and interpretive understanding of the process. To the best of our knowledge, no previous study has reported the exact Ti/$TiO_2$–Ag–Sn/Pb–$PbO_2$ configuration for the EO of PS NPs.

## 2. Materials and methods

### 2.1. Materials

All reagents were used as received at the stated purities. For NP synthesis, styrene monomer (≥99%, inhibitor-stabilized), divinylbenzene, sodium dodecyl sulfate (SDS, ≥99%), and potassium persulfate (KPS, ≥99%) were used. For the interlayer and coating, titanium(IV) isopropoxide (TTIP, ≥97%), glacial acetic acid (≥99.7%), silver nitrate ($AgNO_3$, ≥99.9%), tin(II) nitrate ($Sn(NO_3)_2$, ≥98%), and metallic lead sheets (Pb, ≥99.9%) were used. Electrolytes and pretreatment chemicals included sodium sulfate ($Na_2SO_4$, ≥99%), sodium phosphate ($Na_3PO_4$, ≥98%), sodium hydroxide (NaOH, ≥98%), sodium carbonate ($Na_2CO_3$, ≥99.5%), nitric acid ($HNO_3$), and oxalic acid (≥99%). Acetone (≥99.5%) and deionized water (18.2 MΩ·cm) were used for cleaning and solution preparation. High-purity nitrogen gas (99.99%) was used for purging and maintaining inert conditions during polymerization.

### 2.2. Synthesis of polystyrene nanoplastics

PS NPs were synthesized by emulsion polymerization [38, 39], as shown in Figure 1a. According to this figure, a 500 mL three-neck round-bottom flask was immersed in a silicone oil bath. To prevent solvent loss, a reflux condenser was connected to the flask. The reaction mixture consisted of 20 g of styrene monomer, DVB as a cross-linker, and 360 mg of surfactant SDS, all dissolved in 250 mL of deionized water. The mixture was maintained at 70 ºC and stirred at 250 rpm for 5 hours, with the temperature kept constant. A thermometer was used to ensure the solution temperature remained constant. To initiate polymerization, KPS was added as an initiator while nitrogen gas was used to purge the system. The mixture was then allowed to cool to room temperature and sonicated with a probe processor for 15 min [40].

### 2.3. Preparation of Ti/$TiO_2$-Ag-Sn/Pb-$PbO_2$ composite electrode

#### 2.3.1. Preparation of the threaded titanium rod

To prepare metal oxide films with strong adhesion, high-purity threaded titanium rods served as the electrode substrate. The treatment process began by polishing the rods with 600-mesh abrasive paper, followed by separate 30-minute cleaning steps using deionized water and acetone. After cleaning, the rods were etched in a solution containing 0.3 M $Na_3PO_4$, 1.2 M NaOH, and 0.2 M

$Na_2CO_3$ at 45°C for 30 minutes. Once removed, they were submerged in a 50% $HNO_3$ solution heated to 85°C for an hour, resulting in gray, roughened titanium surfaces. Finally, the rods were washed with deionized water and then stored in a 10% oxalic acid solution by weight.

### 2.3.2. Synthesis of the $TiO_2$/Ag-Sn interlayer

A $TiO_2$/Ag-Sn interlayer was synthesized by a sol-gel technique, using TTIP as the titanium precursor. First, 8.95 mL of $CH_3COOH$ was placed in a 200 mL beaker and cooled in an ice water bath. Then, 4.65 mL of TTIP was added to the cooled mixture, followed by vigorous stirring for 30 minutes until a sol was formed. Next, 5 mg of $AgNO_3$ and 5 mg of $Sn(NO_3)_2$ were dissolved in 98.75 mL of deionized water. This solution was added dropwise to the TTIP mixture under continuous stirring for 4.5 h. After stirring, the solution underwent a 15-minute sonication process. Finally, the resulting mixture was left undisturbed for 24 hours in a dark environment at room temperature.

### 2.3.3. Preparation of the Ti/$TiO_2$/Ag-Sn electrode

In the next step, a Ti/$TiO_2$/Ag-Sn electrode was fabricated through an electrodeposition process. The electrodeposition solution contained the synthesized $TiO_2$/Ag-Sn mixture. The Ti electrode served as the cathode and a Ti mesh as the anode, with the process running for 3 minutes at a current density of 10 mA/$cm^2$. After deposition, the Ti/$TiO_2$/Ag-Sn electrode was rinsed thoroughly with distilled water and calcined in a furnace at 505 °C. This electrodeposition and calcination procedure was repeated three times. Ti/$TiO_2$/Ag and Ti/$TiO_2$/Sn electrodes were also fabricated using the same electrodeposition technique. However, the key variation was the utilization of $TiO_2$/Ag and $TiO_2$/Sn solutions for the respective electrode preparations.

### 2.3.4. Preparation of the Ti/$TiO_2$/Ag-Sn/Pb-$PbO_2$ electrode

In the final step, the TASP electrode was fabricated. This was achieved by depositing molten Pb onto the Ti/$TiO_2$/Ag-Sn electrode through a dip-coating method. For this purpose, the Pb sheets were cleaned, dried at 105 °C for 15 minutes, and then heated in a furnace at 350 °C for 20 minutes to form the molten solution for dip-coating. After dip-coating, the electrode was polished and threaded to standardize and increase the surface area. After the Pb layer deposition, the TASP electrode underwent an oxidation process in a solution of 0.1 M $Na_2SO_4$. The oxidation process

was carried out for 2 hours at a current density of 1 mA/cm², with the TASP electrode as the anode and a stainless-steel electrode as the cathode. Then, the electrode was washed thoroughly with distilled water and calcined in a furnace at 280 °C for 2 hours. This sequence of oxidation and calcination was repeated three times. Figure 1b shows the preparation procedure for the TASP threaded electrode.

### 2.4. Characterization of the prepared polystyrene and electrode

The surface morphology and composition of the fabricated electrodes and PS NPs were analyzed by field-emission scanning electron microscopy (FE-SEM, TESCAN MIRA3) and energy-dispersive X-ray spectroscopy (EDS). Dynamic light scattering (DLS) was used to evaluate particle size. Moreover, the structural properties and crystalline phases of the synthesized electrodes were determined by X-ray diffraction (XRD). XRD patterns were obtained from powdered samples using CuKα radiation (wavelength = 0.154 nm) and scanned over a broad angular range (2θ = 20–80°) on an X-ray diffractometer (XRD Philips PW1730). The functional groups in the synthesized components were identified through Fourier-transform infrared spectroscopy (FTIR) using a Varian Cary Eclipse from Agilent. Furthermore, the degradation of PS nanoparticles was tracked using a JASCO V-730 UV–Vis spectrophotometer with diffuse reflectance spectroscopy (DRS).

Moreover, in this study, electrochemical measurements, including electrochemical impedance spectroscopy (EIS) and polarization curves, were conducted. A three-electrode arrangement was utilized, where a stainless-steel electrode acted as the counter electrode, the prepared electrodes functioned as the working electrode, and a saturated calomel electrode (SCE) was used as the reference.

### 2.5. Electrooxidation process for degradation of polystyrene

Figure 1c depicts an electrolytic setup in which an electrochemical cell was placed on a magnetic stirrer, with a DC power supply providing the electrical energy to drive the electrochemical reactions. In this setup, the prepared electrodes served as the anode, and a stainless-steel mesh electrode served as the cathode. A cylindrical brass ring connected the anode to the power supply, with insulation provided by a plastic piece to separate the electrode from the overhead stirrer. The overhead stirrer rotated the anode at a controlled speed of 200 rpm. Additionally, the magnetic

stirrer continuously mixed the PS NPs wastewater during the degradation process.

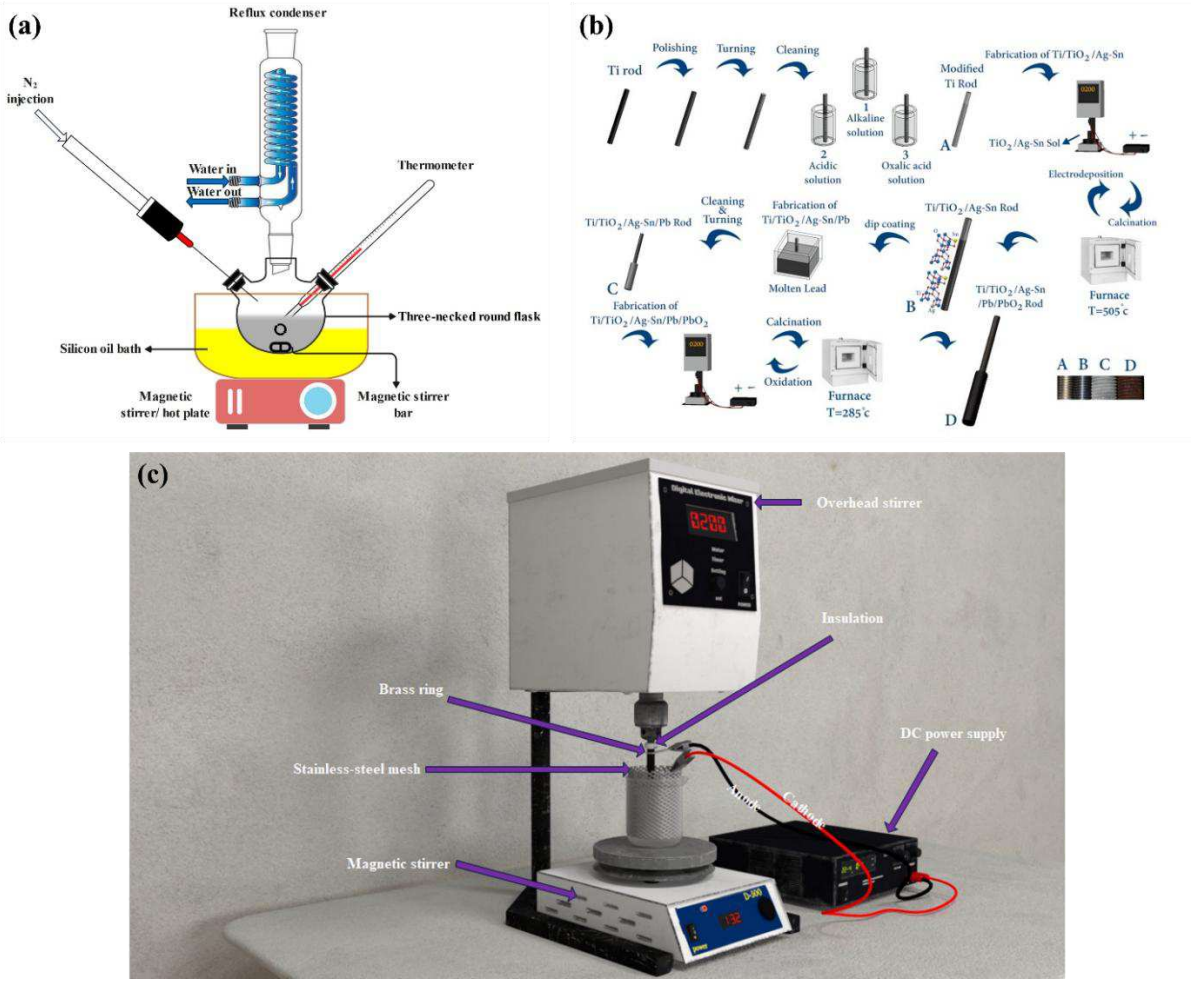



Figure 1. Schematic diagram of (a) the synthesis procedure of the PS NPs; (b) preparation procedure of the TASP threaded electrode; (c) the proposed electrochemical setup for degradation of PS NPs.

To prepare the simulated wastewater with PS NPs, 100 mL of a PS NPs solution and $Na_2SO_4$ electrolyte were added to the electrolytic cell. The degradation efficiency of the PS NPs was measured at 30-minute intervals, and was calculated as follows:

$$\eta\,(\%) = {}^{(A_0 - A_t)}/_{A_0} \times 100 \qquad (1)$$

In this equation, $A_0$ and $A_t$ represent the initial and final absorbance intensity of the PS NPs, respectively.

## 2.6. Design and analysis of experiments

A maximin LHS design augmented with a two-level factorial was used to evaluate the effects of pH (A), initial PS-NP concentration (B), and current density (C) on removal efficiency. The factor ranges were pH 3–10, initial concentration 20–50 ppm, and current density 4.5–13.5 $mA \cdot cm^{-2}$. The maximin criterion maximizes the minimum pairwise distance between design points, thereby promoting an even spread across the design space [41]. The LHS component was generated with a shrinkage factor of 0.9 to avoid excessive clustering near the boundaries and supplied 44 interior points. Because the optimum was expected to lie near the boundary of at least one factor, a two-level factorial augmentation was added as 8 boundary points. Four center-point replicates were also included to estimate pure error. The combined design therefore comprised 44 LHS points, 8 factorial points, and 4 center points, giving a total of 56 runs. Both the RSM and ANN-PSO models were then fitted to this dataset and compared. The full run order and the measured and predicted responses are presented in Table 1.

Table 1. Maximin LHS, two-level factorial, and center-point design with measured and predicted PS-NP removal efficiencies from RSM and ANN-PSO models.

| Run # | Independent variables | | | Removal efficiency (%) | | |
|---|---|---|---|---|---|---|
| | pH | Initial concentration (ppm) | Current density ($mA \cdot cm^{-2}$) | Experiment | ANN-PSO model | RSM model |
| 1 | 3.0 | 20.0 | 4.5 | 64.1 | 67.6 | 67.0 |
| 2 | 3.0 | 20.0 | 13.5 | 78.8 | 78.3 | 77.1 |
| 3 | 3.0 | 50.0 | 4.5 | 49.5 | 54.5 | 46.9 |
| 4 | 3.0 | 50.0 | 13.5 | 58.8 | 61.4 | 57.0 |
| 5 | 10.0 | 20.0 | 4.5 | 83.0 | 82.3 | 81.2 |
| 6 | 10.0 | 20.0 | 13.5 | 85.1 | 86.3 | 83.0 |
| 7 | 10.0 | 50.0 | 4.5 | 61.7 | 61.0 | 61.0 |
| 8 | 10.0 | 50.0 | 13.5 | 63.5 | 65.1 | 62.8 |
| 9 | 7.0 | 23.3 | 10.35 | 90.8 | 90.4 | 93.0 |
| 10 | 6.05 | 24.1 | 5.25 | 88.6 | 84.5 | 86.6 |
| 11 | 9.05 | 30.6 | 8.9 | 86.1 | 84.6 | 84.7 |

| | | | | | | |
|---|---|---|---|---|---|---|
| 12 | 6.6 | 33.4 | 6.05 | 86.4 | 85.9 | 84.1 |
| 13 | 4.85 | 40.6 | 10.6 | 73.5 | 74.5 | 77.3 |
| 14 | 9.55 | 37.0 | 7.55 | 76.0 | 75.9 | 77.6 |
| 15 | 5.55 | 24.8 | 11.1 | 89.2 | 89.9 | 90.2 |
| 16 | 7.3 | 32.2 | 7.75 | 90.0 | 88.6 | 87.1 |
| 17 | 6.25 | 41.6 | 12.25 | 79.5 | 84.4 | 81.5 |
| 18 | 6.5 | 43.7 | 5.4 | 77.4 | 78.5 | 75.3 |
| 19 | 3.55 | 47.6 | 9.2 | 62.4 | 61.9 | 61.5 |
| 20 | 6.15 | 40.1 | 10.85 | 84.7 | 85.4 | 82.3 |
| 21 | 9.25 | 26.7 | 6.65 | 86.1 | 85.7 | 84.6 |
| 22 | 5.85 | 22.6 | 12.95 | 90.7 | 90.4 | 92.2 |
| 23 | 4.65 | 28.9 | 9.0 | 81.5 | 84.4 | 82.9 |
| 24 | 8.2 | 27.8 | 6.25 | 86.1 | 86.8 | 87.1 |
| 25 | 4.3 | 38.1 | 12.4 | 72.8 | 72.1 | 77.0 |
| 26 | 5.25 | 42.6 | 8.55 | 78.2 | 75.5 | 76.0 |
| 27 | 4.95 | 46.9 | 11.8 | 66.9 | 67.9 | 72.7 |
| 28 | 7.65 | 46.0 | 10.1 | 75.4 | 77.3 | 77.5 |
| 29 | 8.05 | 46.4 | 6.95 | 72.8 | 75.2 | 74.6 |
| 30 | 5.2 | 25.8 | 12.6 | 90.3 | 89.2 | 88.8 |
| 31 | 9.5 | 31.0 | 11.5 | 82.4 | 80.8 | 82.3 |
| 32 | 4.05 | 34.7 | 9.5 | 70.5 | 72.0 | 76.1 |
| 33 | 4.45 | 43.5 | 7.2 | 66.2 | 65.4 | 69.5 |
| 34 | 4.1 | 35.5 | 7.5 | 75.5 | 70.0 | 73.8 |
| 35 | 8.4 | 38.0 | 8.2 | 80.8 | 81.9 | 81.9 |
| 36 | 8.25 | 22.0 | 4.95 | 79.7 | 84.5 | 88.0 |
| 37 | 7.4 | 42.3 | 6.6 | 84.4 | 82.2 | 78.7 |
| 38 | 3.9 | 23.2 | 7.1 | 82.6 | 80.1 | 78.3 |
| 39 | 3.7 | 35.9 | 6.1 | 65.9 | 62.4 | 68.4 |
| 40 | 7.9 | 34.3 | 9.7 | 86.0 | 86.6 | 86.3 |
| 41 | 8.55 | 28.5 | 11.4 | 88.8 | 87.2 | 88.1 |
| 42 | 8.9 | 39.2 | 10.75 | 75.3 | 76.6 | 79.9 |
| 43 | 6.75 | 31.5 | 9.8 | 90.8 | 89.5 | 88.7 |
| 44 | 6.9 | 25.9 | 8.3 | 90.7 | 90.0 | 90.8 |
| 45 | 5.65 | 33.1 | 8.7 | 85.5 | 87.5 | 84.7 |

| | | | | | | |
|---|---|---|---|---|---|---|
| 46 | 5.5 | 45.2 | 5.75 | 67.8 | 69.8 | 71.4 |
| 47 | 3.4 | 47.9 | 12.7 | 65.0 | 61.8 | 62.3 |
| 48 | 7.2 | 44.5 | 12.05 | 81.5 | 80.4 | 79.5 |
| 49 | 8.7 | 39.5 | 5.65 | 76.7 | 76.8 | 77.7 |
| 50 | 4.5 | 29.7 | 11.6 | 85.3 | 83.3 | 83.3 |
| 51 | 7.55 | 36.7 | 7.9 | 83.8 | 86.5 | 84.1 |
| 52 | 9.1 | 27.2 | 10.2 | 84.4 | 86.3 | 86.5 |
| 53 | 6.5 | 35.0 | 9.0 | 88.5 | 88.5 | 85.8 |
| 54 | 6.5 | 35.0 | 9.0 | 87.4 | 88.5 | 85.8 |
| 55 | 6.5 | 35.0 | 9.0 | 89.6 | 88.5 | 85.8 |
| 56 | 6.5 | 35.0 | 9.0 | 89.3 | 88.5 | 85.8 |

### 2.6.1. Response surface methodology

A second-order response surface was fitted to the experimental data in Table 1 to relate removal efficiency ($Y$) to the coded factors $x_A$(pH), $x_B$(initial PS-NP concentration), and $x_C$(current density). The quadratic RSM followed the standard polynomial form [42]:

$$Y = \beta_0 + \beta_A x_A + \beta_B x_B + \beta_C x_C + \beta_{AA} x_A^2 + \beta_{BB} x_B^2 + \beta_{CC} x_C^2 + \beta_{AB} x_A x_B + \beta_{AC} x_A x_C + \beta_{BC} x_B x_C \quad (2)$$

In this equation, $\beta_0$ is the intercept, $\beta_A, \beta_B, \beta_C$ are the linear (main-effect) coefficients, $\beta_{AA}, \beta_{BB}, \beta_{CC}$ are the quadratic (curvature) coefficients, and $\beta_{AB}, \beta_{AC}, \beta_{BC}$are the two-factor interaction coefficients [43].

### 2.6.2. Artificial neural network model

An ANN was developed as a data-driven surrogate to predict removal efficiency from the three coded inputs $x_A$ (pH), $x_B$ (initial concentration), and $x_C$ (current density). A three-layer, feed-forward topology was used with three input nodes, a single hidden layer of three neurons, and one linear output neuron. Inputs and output were normalized to the range −1 to 1 to avoid scaling effects. Hidden units used a hyperbolic tangent sigmoid activation, and network parameters (weights and biases) were optimized using PSO, with mean squared error as the objective function. Hereafter, this model is referred to as the ANN-PSO model. The PSO implementation used a

population size of 50 particles and a maximum of 100 iterations; the inertia weight was initially set to 1 and gradually decreased using a constant damping factor ($W_{damping}$ = 0.99), yielding the optimal weights and biases upon convergence. The dataset in Table 1 was randomly partitioned into training/validation/test subsets in a 70/15/15 split. Model generalization was assessed using the validation subset, and the final model was defined by the PSO solution yielding the lowest validation error [44]. To reduce sensitivity to random initialization, multiple training restarts were performed and the instance with the best validation performance was selected. Model adequacy and generalization were assessed using the coefficient of determination ($R^2$), adjusted coefficient of determination ($R^2_{adj}$), root mean squared error (RMSE), mean absolute error (MAE), and absolute average deviation (AAD) by the following equations [45]:

$$R^2 = 1 - \frac{\sum_{i=1}^{n} \left(y_{i,cal} - y_{i,exp}\right)^2}{\sum_{i=1}^{n} \left(y_{ave,exp} - y_{i,exp}\right)^2} \quad (3)$$

$$R^2_{adj} = 1 - \left[\frac{(1 - R^2)(n-1)}{n - K - 1}\right] \quad (4)$$

$$RMSE = \sqrt{\frac{\sum_{i=1}^{n} \left(y_{i,cal} - y_{i,exp}\right)^2}{n}} \quad (5)$$

$$MAE = \frac{\sum_{i=1}^{n} \left|y_{i,cal} - y_{i,exp}\right|}{n} \quad (6)$$

$$AAD = \frac{1}{n} \sum_{i=1}^{n} \frac{\left|y_{i,cal} - y_{i,exp}\right|}{y_{i,exp}} \times 100 \quad (7)$$

In these expressions, $y_{i,\mathrm{cal}}$, $y_{i,\mathrm{exp}}$, and $\bar{y}_{\mathrm{exp}}$ denote the predicted response for the $i^{\mathrm{th}}$ run, the measured (experimental) response, and the mean of the experimental dataset, respectively. Moreover, $n$ is the number of observations and $K$ is the number of input variables.

### 2.6.3. Genetic algorithm

A GA was implemented in MATLAB R2023b (MathWorks Inc., USA) to optimize the electro-oxidation operating parameters based on the predictive ANN-PSO model. The optimization began with a uniformly distributed initial population of 50 individuals. Stochastic uniform selection was

used to ensure fair sampling and maintain genetic diversity across generations. Offspring were generated by scattered crossover applied to 80% of the population and Gaussian mutation to introduce small random variations for effective exploration of the search space. An elite count equal to 5% of the population was directly transferred to the next generation to preserve the best-performing individuals. The combination of stochastic selection, high crossover probability, Gaussian mutation, and elitism provided a well-balanced exploration–exploitation strategy, ensuring convergence stability and preventing premature convergence during the optimization process.

### 2.6.4. Garson's method

Garson's method estimates the relative importance of each input variable in a feed-forward ANN by partitioning the connection weights linking inputs to the output through the hidden layer [42, 44]. In this study, Garson's method was applied to the trained ANN-PSO model to quantify the contribution of each input parameter. The following equation is used for Garson's method [46]:

$$I_j = \frac{\sum_{m=1}^{m=N_h}\left(\left(\frac{|W_{jm}^{ih}|}{\sum_{k=1}^{k=Ni}|W_{km}^{ih}|}\right)\times|W_{mn}^{ho}|\right)}{\sum_{k=1}^{k=Ni}\left(\sum_{m=1}^{m=N_h}\left(\left(\frac{|W_{km}^{ih}|}{\sum_{k=1}^{k=Ni}|W_{km}^{ih}|}\right)\times|W_{mn}^{ho}|\right)\right)} \quad (8)$$

Here, $I_j$ denotes the relative importance of the $j$-th input variable in determining the response. $W$ represents the network connection weights, and $N_i$ and $N_h$ are the numbers of input and hidden neurons, respectively. Superscripts $i$, $h$, and $o$ indicate the input, hidden, and output layers, while subscripts $k$, $m$, and $n$ index individual neurons in the input, hidden, and output layers, respectively.

## 2.7. Electrical energy per order analysis

To evaluate the energy efficiency of the electro-oxidation process, the electrical energy per order ($E_{EO}$) was calculated for the operating conditions investigated. This section presents the definition of EEO and its mathematical expression used to quantify the energy required for pollutant degradation.

This parameter is widely used as a figure of merit for oxidation processes because it directly relates the electrical energy input to the degree of contaminant removal achieved in a given treated

volume. For batch systems, $E_{EO}$ is defined as the electrical energy required to reduce the pollutant concentration by one order of magnitude in one cubic meter of water [47].

$$E_{EO} = \frac{U \times I \times t}{1000V \times log_{10}(^{C_0}/_{C_t})} \quad (9)$$

In this equation, $U$ is the average cell voltage (V), $I$ is the applied current (A), $t$ is the electrolysis time (h), $V$ is the treated solution volume ($m^3$), $C_0$ is the initial pollutant concentration, and $C_t$ is the pollutant concentration after treatment time $t$. The term $log_{10}(^{C_0}/_{C_t})$ expresses the extent of degradation in terms of one-order reduction, while the factor 1000 converts the electrical energy into kWh.

## 3. Results and discussion

### 3.1. Characterization of polystyrene nanoplastics

#### 3.1.1. FE-SEM analysis of polystyrene nanoplastics

Figure 2a shows the morphology and size of the synthesized PS NPs as observed by FE-SEM analysis. The PS NPs appeared as both isolated and aggregated spheres with a uniform spatial distribution. FE-SEM analysis indicated that the particle size ranged from approximately 20 to 40 nm. Additionally, the FE-SEM images revealed a distinct porous structure on the surface of the synthesized PS NPs.

#### 3.1.2. DLS analysis of polystyrene nanoplastics

The DLS results for the synthesized PS NPs are presented in Figure 2b. As shown in the figure, the average particle size of the PS nanoparticles was 52.7 nm, which aligns well with the FE-SEM findings that indicated a particle size range of approximately 20 to 40 nm.

#### 3.1.3. FTIR analysis of polystyrene nanoplastics

Figure 2c shows the FTIR spectrum of PS NPs, which can be divided into three main regions: (1) 500–2000 $cm^{-1}$, (2) 2000–3000 $cm^{-1}$, and (3) 3000–4000 $cm^{-1}$. In the 500 to 2000 $cm^{-1}$ range, peaks between 650 and 900 $cm^{-1}$ are attributed to C–H deformation vibrations, while the 900 to 1250 $cm^{-}$

$^{1}$ range indicates further C–H deformation. The 1475 to 1625 $cm^{-1}$ range reveals C–C stretching, with notable peaks at 1500 and 1600 $cm^{-1}$ associated with aromatic C=C stretching. Peaks between 1650 and 2000 $cm^{-1}$ are attributed to C–H overtone frequencies. In the 2000 to 3000 $cm^{-1}$ range, the peak at 2850.17 $cm^{-1}$ corresponds to aliphatic C–H bonds. The 3000 to 4000 $cm^{-1}$ region includes a peak at 3025.28 $cm^{-1}$, related to aromatic C–H stretching, while peaks at 3059.46 and 3081.68 $cm^{-1}$ correspond to C–H stretching vibrations of ring hydrogens [48].

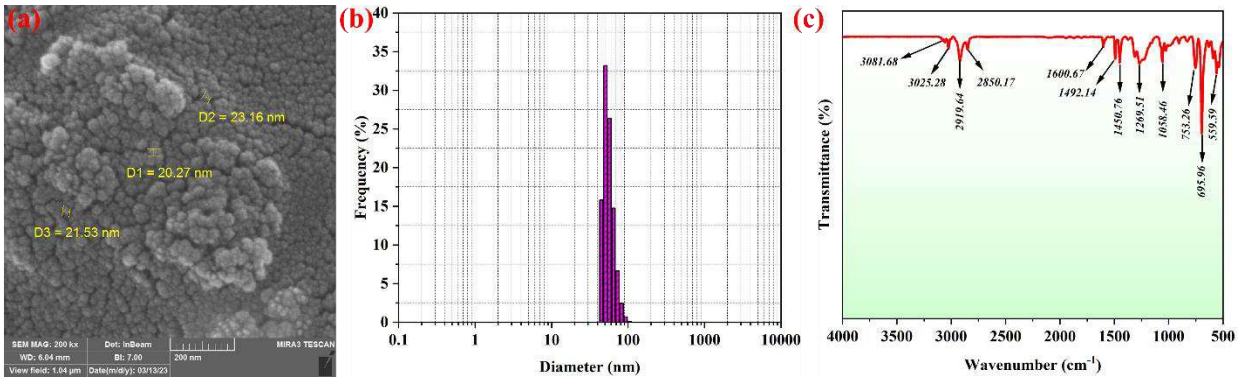



Figure 2. Characterization analyses of synthesized PS NPs a) FE-SEM image, b) DLS particle size distribution, and c) FTIR spectra.

### 3.2. Characterization of threaded electrodes

#### 3.2.1. FE-SEM and EDS characterizations of the electrodes

Figures 3a and 3b show the surface morphology of the fabricated TASP electrode. Figure 3a presents the cross-sectional FE-SEM image of the threaded TASP electrode, showing the well-defined layered architecture of the composite electrode. The titanium substrate served as the base, onto which the $TiO_2$-Ag-Sn interlayer was deposited. This intermediate layer appeared uniform and adherent, forming a crucial interface between the titanium substrate and the subsequently deposited Pb layer. The Pb layer, applied via dip-coating, exhibited a relatively homogeneous thickness, indicating effective deposition. Furthermore, the outermost $PbO_2$ layer, formed by electrochemical oxidation, was evenly distributed, suggesting successful transformation of Pb into its oxidized state.

Moreover, the surface morphology of the $TiO_2$-Ag-Sn intermediate layer is further examined in

Figure 3b, which provides a high-magnification FE-SEM image of the composite structure. The $TiO_2$ matrix exhibited a porous and granular morphology, which increased the electrode's surface area and enhanced catalytic activity. Dispersed within the $TiO_2$ network were Ag and Sn particles, which were clearly distinguishable in the FE-SEM image. Ag and Sn appeared uniformly incorporated into the $TiO_2$ matrix, with no significant agglomeration observed, indicating effective synthesis via the sol-gel method. Furthermore, Figure 3c confirms the successful construction of the multilayer TASP electrode through EDS and elemental mapping analyses. The detected presence of Ti, O, Ag, Sn, and Pb is consistent with the intended electrode architecture and verifies that both the interlayer and outer active layer were successfully formed. More importantly, the elemental maps suggest a relatively uniform distribution of Ag and Sn within the $TiO_2$-based intermediate layer, while Pb and O are continuously distributed over the outer region, indicating $PbO_2$ formation. This homogeneous distribution is significant because it suggests the modifier species were effectively incorporated without obvious phase segregation or localized agglomeration. Such uniformity is expected to promote more even current distribution, reduce local hot spots during EO, improve the accessibility of active sites, and enhance the structural integrity of the coating during operation. Therefore, the elemental mapping results support the improved electrochemical performance and durability later observed for the TASP electrode.

### 3.2.2. XRD analysis of the electrodes

The XRD analysis in Figure 3d provides insight into the structural properties of the electrode's active components. For the β-$PbO_2$ coating, seven distinct diffraction peaks appeared at specific angles: 25.40°, 31.98°, 36.11°, 49.13°, 58.79°, 62.43°, and 66.70°. These angular positions corresponded to the (110), (101), (200), (211), (310), (301), and (202) planes of the β-$PbO_2$ crystal system [49]. Moreover, the XRD pattern revealed characteristic $TiO_2$ peaks at $2\theta = 25.26°$ (101), 37.79° (004), 48.08° (200), 54.03° (105), 55.15° (211), 62.70° (204), and 68.80° (116) [50]. Metallic Ag was identified by peaks at $2\theta = 38.21°$ (111), 44.65° (200), and 64.88° (220) [51], while Sn appeared at 30.58° (200) and 32.12° (101) [52]. The absence of secondary phases (e.g., $SnO_2$ or $Ag_2O$) suggests successful doping without oxidation during synthesis.

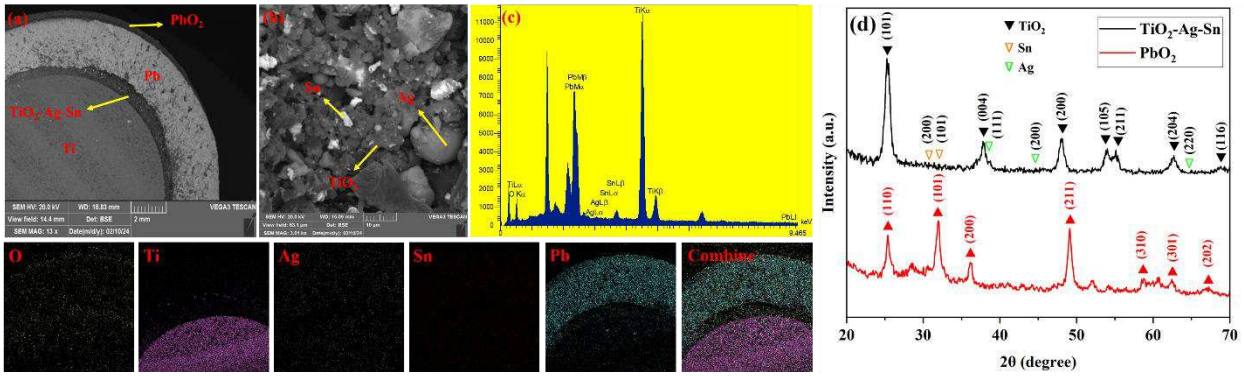



Figure 3. FE-SEM images of (a) TASP electrode and (b) $TiO_2$-Ag-Sn intermediate layer; (c) EDS pattern and representative element distribution images of the TASP electrode; (d) XRD patterns of the $PbO_2$ and $TiO_2$-Ag-Sn intermediate layer.

### 3.2.3. Electrochemical performance of the electrodes

Figure 4a shows the linear sweep voltammetry (LSV) results for the Ti/$TiO_2$/Pb-$PbO_2$ (TP), TASP, Ti/$TiO_2$/Ag/Pb-$PbO_2$ (TAP), and Ti/$TiO_2$/Sn/Pb-$PbO_2$ (TSP) electrodes, conducted at a scan rate of 50 mV $s^{-1}$ in 0.1 M phosphate buffer solution. The oxygen evolution potentials (OEPs), defined as the onset of rapid current increase due to oxygen evolution, were determined to be 1.55 V, 1.97 V, 1.74 V, and 1.63 V vs. Ag/AgCl for TP, TASP, TAP, and TSP, respectively. In the electrochemical degradation of pollutants, a higher OEP is advantageous because it suppresses the competing oxygen evolution reaction (OER), thereby enhancing the current efficiency toward organic oxidation [53, 54]. The TASP electrode, with the highest OEP (1.97 V), showed the greatest ability to delay OER, favoring the generation of reactive oxygen species such as hydroxyl radicals (•OH) essential for pollutant degradation [55]. These results indicate that incorporating Ag and Sn into the $PbO_2$ layer significantly raises the OEP, mitigating the detrimental effects of OER and improving the overall electrochemical oxidation performance.

Figure 4b shows the Tafel polarization curves for TP, TASP, TAP, and TSP electrodes measured in 0.1 M $Na_2SO_4$ solution at a scan rate of 50 mV $s^{-1}$ to evaluate their corrosion behavior. All electrodes exhibited stable Tafel profiles, indicating consistent electrochemical stability under the test conditions [56]. Among the electrodes tested, the TASP electrode showed the lowest corrosion current density (0.1437 μA $cm^{-2}$) and the highest corrosion potential (0.12 V), suggesting superior resistance to electrochemical degradation. The TP electrode, by contrast, showed a higher

corrosion current density (1.4374 μA $cm^{-2}$) and a more negative corrosion potential (−0.27 V), indicating lower corrosion resistance. These results highlight the effectiveness of Ag-Sn modification in enhancing the stability and corrosion protection of $PbO_2$-based electrodes.

Figure 4c presents the Nyquist plots for the base TP electrode and the modified TASP electrode. Both electrodes exhibited a depressed semicircular arc in the high- to mid-frequency range, characteristic of charge-transfer processes at the electrode–electrolyte interface. The semicircle of the modified electrode was notably smaller, indicating a lower charge transfer resistance compared to the base electrode [57]. This suggests enhanced charge transfer kinetics, likely because of improved surface conductivity and increased active sites provided by the Ag-Sn doping. In the low-frequency region, both curves transitioned into a linear portion corresponding to Warburg impedance behavior. This linear tail reflects semi-infinite diffusion of electrolyte ions toward the electrode surface; accordingly, a Warburg element was included in the equivalent circuit model to describe this diffusion process [58]. The presence of this linear segment confirms that ion diffusion plays a significant role in the overall impedance response, particularly at low frequencies [59].

Figure 4d presents the cyclic voltammetry (CV) profiles for the TP and TASP electrodes measured in 0.1 M sodium sulfate at a scan rate of 3 mV $s^{-1}$. The TASP electrode exhibited a clear oxidation peak at 0.860 V with a peak current of 6.89 mA, indicating strong redox activity. Such a distinct peak suggests that the electrode surface contains electrochemically active sites that readily participate in reversible redox reactions. In contrast, the TP electrode showed only a weak, broad oxidation response, with a barely noticeable peak around 0.97 V. This weaker signal indicates slower charge transfer and fewer accessible redox-active sites on the electrode surface. The improved electrochemical response of the TASP electrode can be attributed to its modified composite structure. This structure likely enhances electrical conductivity and facilitates more efficient electron transport across the electrode interface. As a result, the presence of additional conductive pathways and active sites enables faster charge transfer and stronger redox behavior compared with the TP electrode.

Figure 4e shows the results of accelerated service life tests conducted on TP, TASP, TAP, and TSP electrodes at a current density of 318 mA $cm^{-2}$ to evaluate their durability. Electrode stability is a critical factor for practical and industrial electrochemical applications, particularly under high-current conditions [60, 61]. The TASP electrode, modified with Ag and Sn, exhibited a markedly extended accelerated service life of 188 s under harsh test conditions, compared with only 45 s for

the unmodified TP electrode under the same conditions. The TAP and TSP electrodes exhibited intermediate lifetimes, reflecting the individual contributions of Ag and Sn, respectively. The enhanced durability of the TASP electrode could be attributed to a synergistic effect between Ag and Sn: silver improves electrical conductivity and promotes uniform current distribution, reducing local degradation, while tin enhances mechanical stability and adhesion, mitigating stress-induced delamination. In contrast, the TP electrode's early failure was attributed to insufficient conductivity and weaker coating integrity, resulting in faster degradation under electrochemical stress.

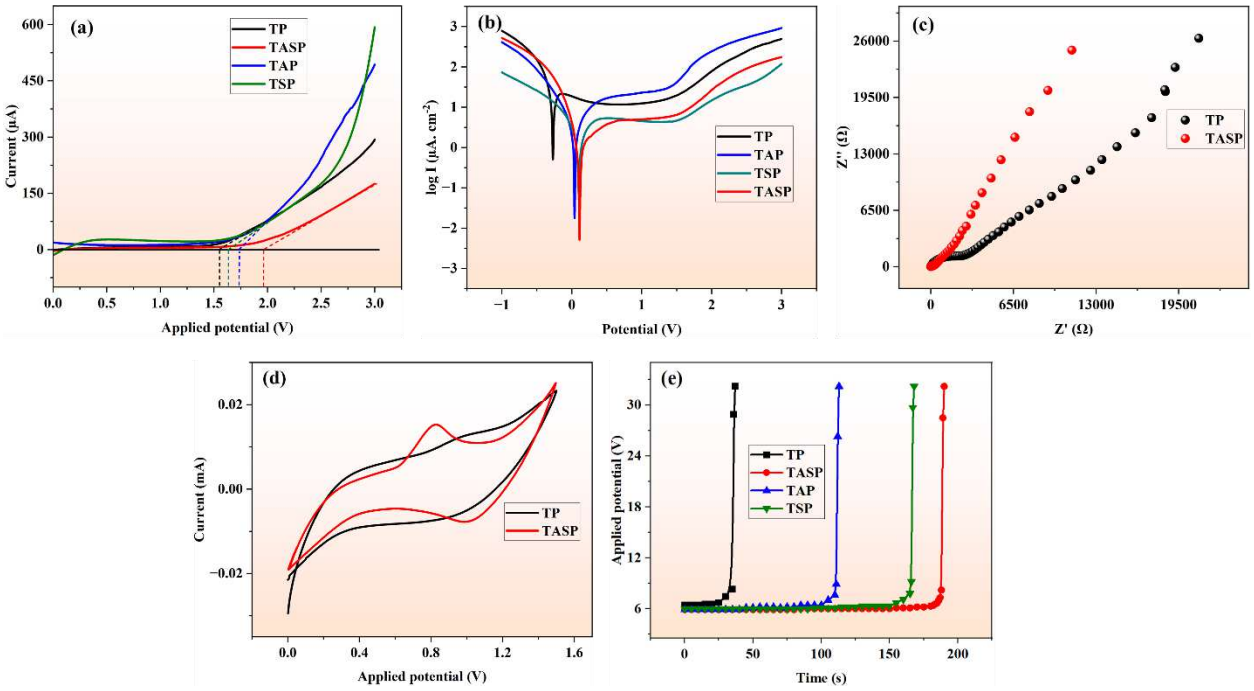



Figure 4. (a) LSV curves of TP, TASP, TAP, and TSP electrodes measured in 0.1 M phosphate buffer solution at a scan rate of 50 mV $s^{-1}$; (b) Tafel curves of TP, TASP, TAP, and TSP electrodes recorded at a scan rate of 50 mV/s; (c) Nyquist plots of TP and TASP electrodes; (d) CV curves of TP and TASP electrodes measured in 0.1 M $Na_2SO_4$ solution at a scan rate of 3 mV $s^{-1}$; and (e) Accelerated service life tests for TP, TASP, TAP, and TSP electrodes conducted at a current density of 318 mA $cm^{-2}$.

### 3.3. Modeling

#### 3.3.1. RSM model

The RSM model obtained for PS-NP electro-oxidation is presented in Eq. (10). Only the statistically significant interaction ($x_A x_C$) was retained in the final reduced quadratic model. The corresponding ANOVA results are summarized in Table S1. The model was statistically significant ($p < 0.0001$), confirming that the selected operating variables collectively exert a meaningful effect on removal efficiency within the studied domain. The coefficient of determination ($R^2 = 0.919$) indicates that the quadratic model explains a large proportion of the experimental variability. The adjusted coefficient of determination ($R^2_{adj} \approx 0.907$) remains close to $R^2$, suggesting that the included terms contribute meaningfully to the model without excessive overparameterization. However, the statistically significant lack-of-fit ($p = 0.04$) indicates that the quadratic polynomial does not fully capture the response behavior across the entire design space. This suggests the presence of more complex nonlinear relationships among pH, initial concentration, and current density than can be adequately represented by a second-order polynomial. Therefore, although the RSM model is useful for identifying general trends, curvature, and factor interactions, its predictive capability is limited compared with those of more flexible nonlinear modeling approach.

$$Y = 14.95 + 17.38x_A + 0.18x_B + 3.38x_C - 1.13x_A^2 - 0.01x_B^2 - 0.10x_C^2 - 0.13x_A x_C \quad (10)$$

#### 3.3.2. ANN-PSO model

Several feed-forward neural networks with a single hidden layer containing different numbers of neurons were trained and validated using the experimental dataset. The optimal architecture (3–3–1) was selected based on the lowest validation error. The final ANN-PSO model achieved $R^2 = 0.953$, $R^2_{adj} = 0.950$, RMSE = 2.125, MAE = 1.678, and AAD = 2.241 on the entire dataset, indicating strong agreement between predicted and experimental removal efficiencies. The corresponding training, validation, and test $R^2$ values were 0.960, 0.943, and 0.907, respectively. The small difference between $R^2$ and $R^2_{adj}$ suggests that the model retained high explanatory power without unnecessary complexity. In addition, the use of separate training, validation, and test subsets, together with multiple training restarts, reduced sensitivity to random initialization and improved model robustness. The final model was selected based on the lowest validation error,

which supports its generalization ability rather than simple memorization of the training data. Therefore, the ANN-PSO model provides accurate interpolation within the studied design space; however, due to the limited size of the experimental dataset, its broader generalization capability should be treated with caution. The optimized connection weights and bias values are summarized in Table S2.

The selected 3–3–1 topology contains 16 adjustable parameters: input-to-hidden weights, hidden-layer biases, hidden-to-output weights, and output bias. For this reason, the final ANN structure was not selected solely on the basis of the coefficient of determination, but rather according to the minimum validation error among the candidate network configurations.

### 3.3.3. Comparison of RSM and ANN-PSO models

The predictive performance of the RSM and ANN-PSO models were evaluated using $R^2$, $R^2_{adj}$, *RMSE, AAD,* and *MAE*, as summarized in Table 2. In all cases, the ANN-PSO model outperformed the RSM model. Its higher $R^2$ (0.953) and $R^2_{adj}$ (0.950) values indicate that it explains a larger fraction of the response variability and retains that explanatory power after accounting for the number of predictors. At the same time, the substantially lower RMSE (2.125), MAE (1.678), and AAD (2.241) values demonstrate that the ANN-PSO predictions deviate less from the experimental observations on average and are therefore more accurate and stable. By contrast, the higher error values obtained for the RSM model, together with its significant lack-of-fit, confirm that the quadratic polynomial cannot fully describe the nonlinear behavior of the electro-oxidation process. These statistical results indicate that the response of PS-NP removal efficiency to pH, current density, and initial concentration is more complex than a second-order surface can represent. Therefore, the ANN-PSO model provides not only better numerical accuracy but also stronger generalization for process prediction and optimization.

Figure 5 compares the experimental removal efficiencies with the values predicted by the RSM and ANN-PSO models. It is evident that the ANN-PSO predictions are more closely clustered around the 1:1 line, indicating better agreement with the experimental data over the studied operating range. In contrast, the RSM model exhibits wider scatter and more noticeable deviations for several runs, suggesting that the quadratic polynomial form is less capable of representing the nonlinear response behavior of the system. This visual evidence is consistent with the statistical metrics reported in Table 2, where ANN-PSO showed higher values of $R^2$ and $R^2_{adj}$ and lower

*RMSE*, *AAD*, and *MAE* than the RSM model. Figure 5 not only confirms the superior predictive accuracy of ANN-PSO over the RSM model, but also demonstrates its excellent agreement with the experimental data across the investigated operating domain. Overall, while both approaches provide satisfactory fits within the studied operating domain, the ANN-PSO model better captures the nonlinear and complex behavior of the electro-oxidation process, yielding more precise response estimations and enhanced predictive reliability.

Table 2. Comparative predictive performance of ANN-PSO and RSM models.

| Parameter | RSM | ANN-PSO |
|---|---|---|
| $R^2$ | 0.919 | 0.953 |
| $R^2_{adj}$ | 0.907 | 0.950 |
| *RMSE* | 2.77 | 2.125 |
| *AAD* | 2.99 | 2.241 |
| *MAE* | 2.29 | 1.678 |

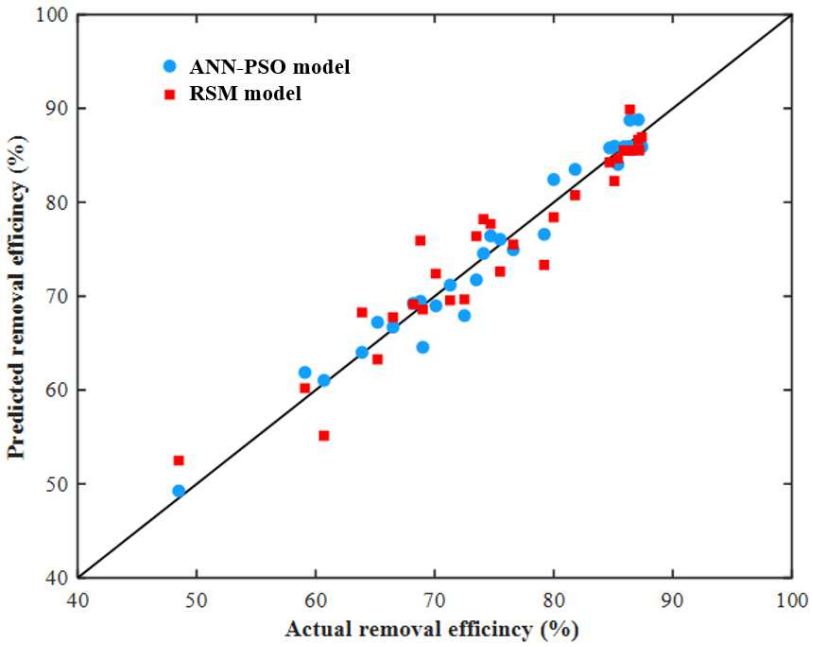



Figure 5. Experimental removal efficiency plotted against predictions from the ANN-PSO and RSM models.

### 3.4. Effects of operating parameters

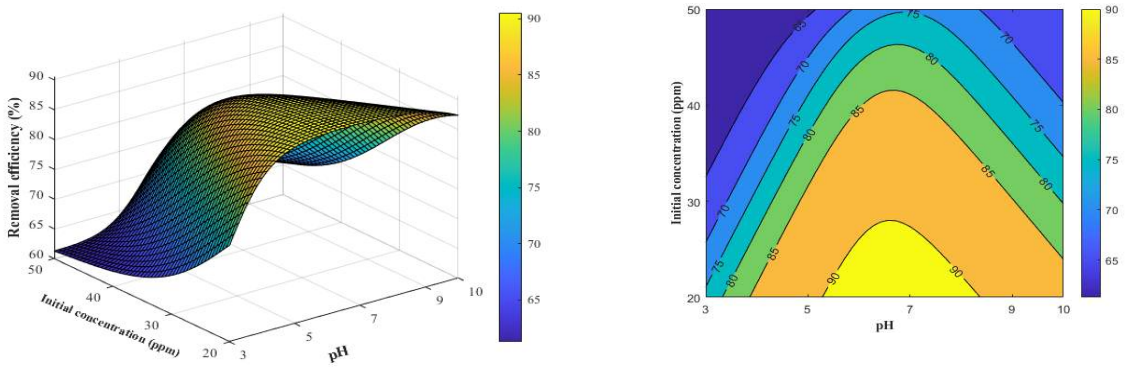
Response surface plots of removal efficiency as functions of the three pairwise combinations, including pH vs. initial concentration, pH vs. current density, and initial concentration vs. current density, are shown in Figure 6. In each plot, the remaining parameter was held constant at its midpoint level (pH = 6.5, $C_0$= 35 ppm, $j$= 9 mA·cm$^{-2}$). Accordingly, each surface passes through the design center, where the measured removal efficiency is approximately 86%. To facilitate comparison of factor interactions and visualize how each pair influences the operating optimum, the corresponding two-dimensional effect plots are provided in Figures S1 to S3, constructed under the same convention of holding the third factor at its midpoint.

#### 3.4.1. Effect of initial concentration

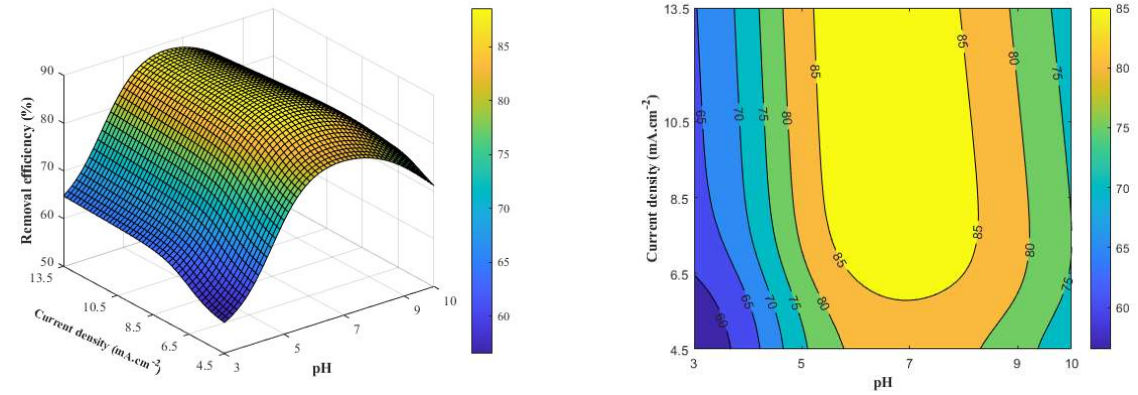
ANN-PSO based response surfaces (Figures 6a and S1) show a pronounced inverse dependence of percentage removal on the initial PS-NP concentration within the studied bounds. Holding the other factors at their design midpoints (pH = 6.5 and $j = 9$ mA·cm$^{-2}$), increasing $C_0$ from 20 to 50 ppm lowered the predicted removal efficiency from 90.5% to 73.7%, a reduction of 16.8 percentage points across the range. This decline reflects an oxidant-limited regime in which a higher pollutant-to-radical ratio reduces the fraction degraded over a fixed treatment time [62, 63]. Thus, any shift toward higher influent loads should be paired with compensating adjustments (e.g., higher current density or longer residence time) to maintain target removal levels.

Comparable trends are widely reported in electro-oxidation studies. Liu et al. [17] examined chloramphenicol degradation on Ti/$PbO_2$-based anodes and showed that raising the initial concentration from 5 to 50 mg L$^{-1}$ progressively decreased both the degradation ratio and TOC removal. Moreover, Bouya et al. [64] investigated 2-nitrobenzaldehyde on BDD anodes and found that while overall oxidation was attainable, the time required for complete removal increased with initial concentration, which they attributed to the larger organic load. Consistent with these findings, a recent study on Rhodamine B using $PbO_2$-based oxidation reported higher removal efficiency at lower initial dye concentrations, attributing the trend to finite oxidant flux and competitive side reactions at elevated loads [65].

(a)




(b)




(c)

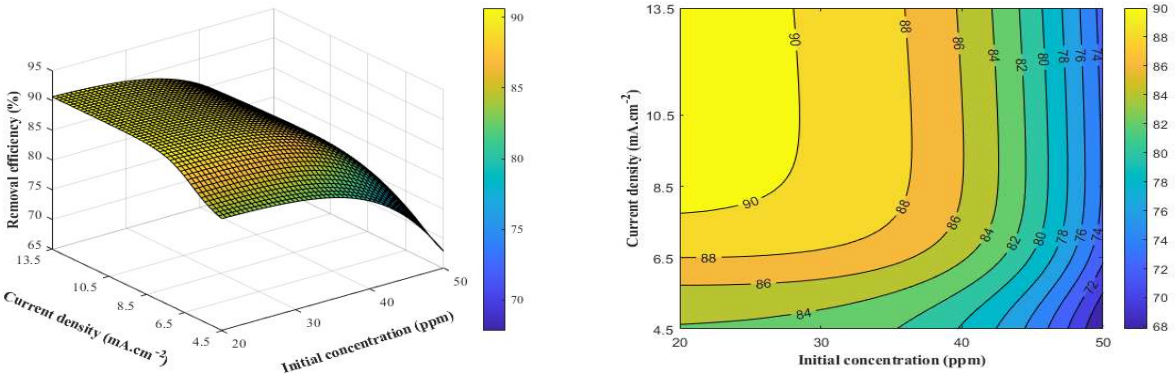



Figure 6. Response surface plots of PS NPs degradation versus paired operating variables: (a) initial concentration and pH; (b) pH and current density; and (c) current density and initial concentration. In all panels, the two variables not varied are held at the midpoints of their respective ranges.

### 3.4.2. Effect of initial pH

Figures 6b and S2 show that ANN-PSO based response surfaces exhibit a bell-shaped dependence of PS-NP removal on pH, with a maximum near neutrality. At the design midpoints ($C_0$ = 35 ppm and $j$ = 9 mA·cm$^{-2}$), the ANN-PSO predicts 63.9% at pH 3, , 88.5% at pH 6.5, and 74.6% at pH 10. The rise from strongly acidic to near-neutral conditions can be attributed to reduced nanoparticle aggregation and more efficient use of oxidizing species [66]. Moreover, excessively low pH may promote corrosion of the $PbO_2$/Ti substrate and surface oxidation that attenuate coating activity, thereby limiting performance [67]. In weakly acidic media (e.g., around pH 5), degradation efficiency tends to remain below the neutral maximum. This is consistent with the notion that proton-rich environments can alter interfacial reactions and diminish the net rate despite moderating oxygen evolution [68]. At higher pH (alkaline conditions), $OH^-$ adsorption on catalytic sites increases. Simultaneously, the oxygen-evolution overpotential decreases (based on Eqs. (11) and (12)), favoring the competing OER, diverting current from pollutant oxidation, and lowering removal efficiency [69].

$$2H_2O \rightarrow 4H^+ + O_2 + 4e^- \quad (11)$$

$$4OH^- \rightarrow 2H_2O + O_2 + 4e^- \quad (12)$$

### 3.4.3. Effect of current density

ANN-PSO based response surfaces (Figures 6c and S3) indicate that removal efficiency increases with current density and then approaches a plateau. At the design midpoints (pH = 6.5 and $C_0$ = 35 ppm), the predicted removal rises from 82.1% at 4.5 mA·cm$^{-2}$ to 88.5% at 9 mA·cm$^{-2}$, but changes only to 88.4% at 13.5 mA·cm$^{-2}$ [70]. The initial gain reflects higher rates of electrogenerated oxidants at the $PbO_2$ surface. Moreover, the near-plateau at higher current densities is consistent with increased oxygen evolution, gas-bubble shielding, site blocking, and transport limitations that cap effective oxidant utilization [71].

This behavior agrees with prior electro-oxidation studies. Zhang et al. [72] synthesized a Ti/$PbO_2$–$Sm_2O_3$ electrode and showed that raising the cell voltage from 2.5 to 3.5 V increased the degradation rate constant of alizarin yellow R from 7.38 × 10$^{-3}$ to 11.08 × 10$^{-3}$ min$^{-1}$. However, performance gains beyond 3.0 V were marginal due to side reactions (notably oxygen evolution),

making 3.0 V as the optimal setting. Furthermore, Zheng et al. [67] synthesized a Ti/La/Co–Sb–$SnO_2$ electrode and reported that, within the current density range of 80–133.33 mA·cm$^{-2}$, the PS degradation rate increased with current density and peaked at 106.67 mA·cm$^{-2}$. However, it subsequently declined at higher current densities, a drop attributed to enhanced oxygen evolution at elevated currents and insufficient electron-transfer rates at lower currents.

### 3.5. Optimization of operating parameters by GA

The operating conditions were optimized by coupling the trained ANN-PSO surrogate model with the GA to maximize removal efficiency within the experimental bounds (pH 3–10, $C_0$ 20–50 ppm, current density 4.5–13.5 mA·cm$^{-2}$). The GA configuration described in Section 2.6.3 was used, and the ANN-PSO predicted removal served as the fitness function under box constraints on each factor. The procedure converged to a solution in the neighborhood of neutral pH, low initial concentration, and upper-mid current density, reflecting the combined effects observed in the response surfaces. As shown in Table 3, the GA-optimized operating conditions were pH = 6.46, initial concentration $C_0$ = 20 ppm, and current density j = 11.44 mA·cm$^{-2}$, with a predicted removal efficiency of 90.64%.

Table 3. Optimal operating conditions obtained by coupling the ANN-PSO surrogate with the GA and the corresponding predicted removal efficiency.

| **Parameter** | **Removal efficiency (%)** | | **pH** | **Initial concentration** | **Current density** |
|---|---|---|---|---|---|
| | Experimental | ANN-PSO model | | | |
| Optimized values | 91.43 | 90.64 | 6.46 | 20.0 | 11.44 |

To further evaluate the practical applicability of the EO process, the electrical energy required to reduce the pollutant concentration by one order of magnitude was determined under optimized operating conditions. The calculated EEO value was 9.65 kWh m$^{-3}$order$^{-1}$, based on Eq. (9). This result indicates that the optimized operating conditions provide high PS-NP degradation with moderate electrical energy demand. Therefore, although the ANN-PSO/GA optimization selected the condition that maximized removal efficiency, the $E_{EO}$ analysis shows that this operating point

remains reasonably acceptable from an energy-performance perspective.

### 3.5.1. Experimental validation and kinetic analysis under optimized conditions

To verify the GA-optimized parameters, degradation experiments were conducted with all electrodes under the identified optimal conditions. Figures 7a and 7b show the time-dependent removal efficiency, revealing that all electrodes followed pseudo-first-order kinetics. The TASP electrode achieved 91.43% PS NPs removal within 90 minutes, demonstrating excellent agreement with the predicted efficiency. The degradation kinetics were analyzed using the pseudo-first-order model ($ln(C_o/C_t) = k_t$). As shown in Figure 7b, the TASP electrode exhibited the highest rate constant (0.0285 $min^{-1}$), approximately 3.2 times that of the unmodified TP electrode (0.00897 $min^{-1}$). The high correlation coefficients ($R^2 > 0.994$) confirm that the pseudo-first-order model adequately describes the degradation process [61]. The superior performance of the TASP electrode under optimized conditions validates both the electrode modification strategy and the ANN-PSO assisted GA optimization framework.

### 3.5.2. Relative importance of the operating parameters

Garson's method, which partitions influence using the neural-network weight matrix, was applied to quantify each input's effect on removal efficiency. Table S2 lists the connection weights and biases for the developed ANN-PSO, and the relative importances computed by Eq. (8) are displayed in Figure 8. Based on this figure, the results show that pH (56.74%) is the dominant factor, followed by initial concentration (29.80%), while current density (13.46%) has the lowest relative contribution within the studied range. This ranking is physically meaningful. pH governs the balance between pollutant oxidation and side reactions such as oxygen evolution, while also affecting interfacial behavior and radical utilization, explaining its dominant influence. The effect of initial concentration is also substantial because pollutant loading influences the oxidant-to-substrate ratio. In contrast, the lower contribution of current density suggests that, within the investigated range, its effect is less dominant than the reaction environment and pollutant loading under the selected conditions. Thus, Figure 8 provides not only a numerical ranking of variable importance but also a useful mechanistic interpretation of the system behavior.

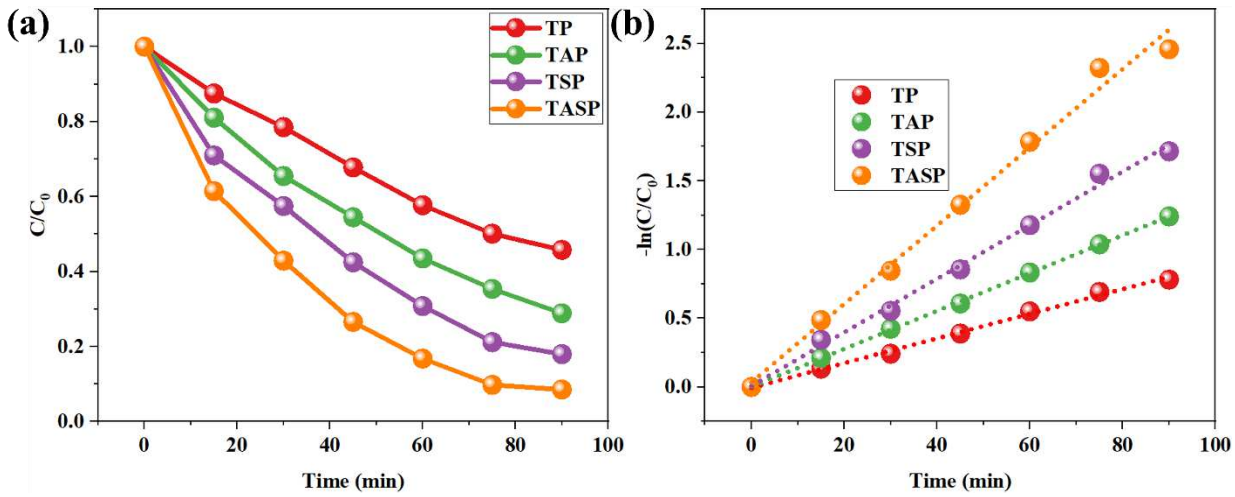



Figure 7. (a) Time-dependent concentration of PS NPs by different electrodes under optimized conditions; (b) Pseudo-first-order kinetic plots for PS NPs electro-oxidation under GA-optimized conditions for different TASP electrodes.

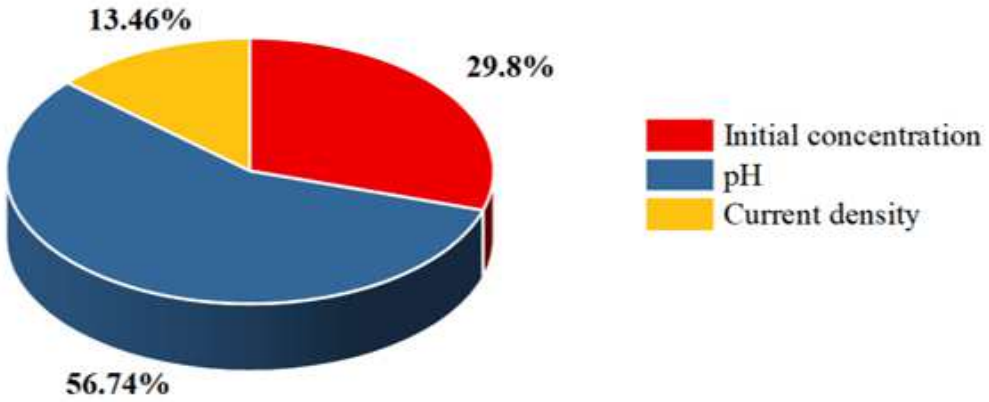



Figure 8. Relative importance of operating parameters on removal efficiency obtained by Garson's method.

### 3.6. Lead leaching analysis

The leaching of lead ions into the treated solution was analyzed by inductively coupled plasma mass spectrometry (ICP-MS, ICPMS7500) under the optimized operating conditions, and the results are shown in Figure S4. The measured $Pb^{2+}$ concentration was 0.009 mg $L^{-1}$ for the unmodified TP electrode and 0.004 mg $L^{-1}$ for the TASP electrode. These results confirm that Ag–Sn modification suppressed lead dissolution during EO. Moreover, the $Pb^{2+}$ concentration

615 measured for the TASP electrode was below the commonly cited drinking-water guideline value
616 of 0.010 mg $L^{-1}$, indicating improved environmental compatibility of the modified anode under
617 the studied conditions [73]. The reduced Pb release is consistent with the enhanced stability of the
618 TASP electrode observed in the electrochemical tests, including its lower corrosion current density
619 and extended service life. Therefore, the ICP-MS results provide direct evidence that the Ag–Sn
620 interlayer not only improves electrochemical performance but also helps mitigate one of the major
621 drawbacks of conventional $PbO_2$-based electrodes.
622

623 **3.7. Proposed degradation mechanism of polystyrene nanoplastics**

624 The EO of PS NPs on the TASP electrode proceeds through three parallel pathways (Figure 9a),
625 dominated by radical-mediated oxidation at the $PbO_2$ surface. The efficiency of these pathways is
626 strongly influenced by the interaction between the multilayer electrode structure and the reaction
627 environment. The Ti substrate provides conductivity and support, while the $TiO_2$–Ag–Sn interlayer
628 enhances coating adhesion, charge transport, and current distribution to the outer Pb/$PbO_2$ layer.
629 These features align with the TASP electrode's higher oxygen-evolution potential, lower
630 charge-transfer resistance, and stronger oxidation response. Thus, they promote the formation and
631 retention of reactive oxidizing species by limiting the competing oxygen-evolution reaction and
632 improving interfacial electron transfer, ultimately increasing both oxidant production and their
633 effective use for PS-NP oxidation.
634 In the primary pathway, hydroxyl radicals ($^{\bullet}OH$) are electrogenerated by anodic water discharge
635 and remain weakly adsorbed on the active layer, forming highly reactive surface species (TASP
636 ($^{\bullet}OH$)). This can be expressed as [74]:

$$TASP + H_2O \rightarrow TASP\,(^{\bullet}OH) + H^+ + e^- \quad (13)$$

637 and equivalently as surface water oxidation:

$$H_2O \rightarrow {}^{\bullet}OH(adsorbed) + H^+ + e^-\,(on\ TASP\ surface) \quad (14)$$

638 These radicals initiate PS oxidation by attacking the polymer backbone, leading to hydroxylation
639 and chain scission, generating smaller aliphatic fragments. With continued oxidation, the aromatic
640 domains are progressively converted to oxygenated intermediates (e.g., catechol-/quinone-type
641 products), followed by ring opening [74]:

$$PS\text{-}(CH_2\text{-}CH(C_6H_5))_n + {}^{\bullet}OH \rightarrow Hydroxylated\ intermediates \rightarrow Chain\ scission \quad (15)$$

$$fragments + Oxidized\ aromatic\ products \rightarrow Ring\text{-}opened\ compounds$$

642 Finally, the resulting low-molecular-weight fragments are further oxidized to carboxylic acids and
643 may undergo further oxidation toward partial mineralization [74]:

$$Aliphatic\ fragments + {}^{\bullet}OH \rightarrow Short\text{-}chain\ carboxylic\ acids \rightarrow CO_2 + H_2O \quad (16)$$

644 Thus, surface-generated ${}^{\bullet}OH$ is the key driver enabling progressive fragmentation and partial
645 mineralization of PS NPs under the optimized operating conditions. A secondary contribution may
646 arise from direct anodic oxidation via interfacial electron transfer, which produces polymer radical
647 cations that undergo bond cleavage [74-76]:

$$PS\text{-}NPs\ (adsorbed) \rightarrow PS\text{-}NPs^{+} + e^{-}\ (direct\ electron\ transfer) \quad (17)$$

$$PS\text{-}NPs^{+} \rightarrow Chain\ scission \rightarrow Fragments \quad (18)$$

648 However, this pathway is expected to be comparatively limited because polystyrene is
649 hydrophobic and non-polar, resulting in weak adsorption on the electrode surface and restricted
650 direct charge transfer; in addition, aromatic rings are partially shielded within the polymer matrix.
651 Therefore, the direct oxidation route likely contributes less than the radical-driven pathway,
652 particularly in systems such as $PbO_2$-based anodes where oxidation proceeds predominantly
653 through generated reactive oxygen species [75].
654 In parallel, the sulfate electrolyte contributes to an important indirect oxidation pathway by
655 generating additional strong oxidants. Sodium sulfate dissociates to sulfate ions, which can be
656 anodically converted to persulfate [76]:

$$Na_2SO_4 \rightarrow 2Na^{+} + SO_4^{2-} \quad (19)$$

$$2SO_4^{2-} \rightarrow S_2O_8^{2-} + 2e^{-} \quad (20)$$

657 followed by activation to sulfate radicals [76]:

$$S_2O_8^{2-} \rightarrow 2SO_4^{\bullet-} \quad (21)$$

658 These $SO_4$ radicals can oxidize PS directly and also regenerate ${}^{\bullet}OH$ through propagation reactions
659 such as [76]:

$$SO_4^{\bullet-} + H_2O \rightarrow {}^{\bullet}OH + SO_4^{2-} + H^{+} \quad (22)$$

$$SO_4^{\bullet-} + OH^{-} \rightarrow {}^{\bullet}OH + SO_4^{2-} \quad (23)$$

while $^{\bullet}OH$ recombination can form hydrogen peroxide: $2^{\bullet}OH \rightarrow H_2O_2$, which further participates in radical production [76]:

$$H_2O_2 + SO_4^{\bullet-} \rightarrow {}^{\bullet}OH + HSO_4^- \quad (24)$$

Consequently, PS degradation may proceed through a cascade involving multiple oxidants [76]:

$$PS\text{-}NPs + SO_4^{\bullet-} \rightarrow Carbon\text{-}centered\ radicals \quad (25)$$

$$PS\text{-}NPs + {}^{\bullet}OH \rightarrow Hydroxylated\ intermediates \quad (26)$$

$$PS\text{-}NPs + H_2O_2 \rightarrow Oxidized\ fragments \rightarrow Progressive\ degradation \rightarrow Mineralization \quad (27)$$

Overall, the coexistence of surface $^{\bullet}OH$, $SO_4^{\bullet-}$, and $H_2O_2$ establishes a synergistic oxidation network that accelerates fragmentation, oxygenation, ring opening, and progressive oxidation of PS NPs, with partial mineralization of the resulting intermediates. This is consistent with the observed pseudo-first-order degradation behavior and high removal efficiency under the optimized conditions. Moreover, operating parameters shape the balance among the key reaction pathways. Increasing current density boosts oxidant generation only up to a moderate level, after which side reactions and bubble formation limit further gains. pH also affects oxidant formation and stability, with near-neutral conditions performing best and strongly acidic or alkaline conditions reducing efficiency. Higher initial PS-NP concentrations lower percentage removal because the same amount of oxidant must be shared across more pollutant molecules. Overall, these trends reflect shifts in oxidant production, consumption, and competition with parasitic reactions.

The high oxygen-evolution potential of the TASP electrode (≈ 1.97 V vs. Ag/AgCl) indicates strong suppression of the competing oxygen evolution reaction and favors the electrogeneration/accumulation of weakly adsorbed $^{\bullet}OH$ on the $PbO_2$ surface. This electrochemical feature directly supports Pathway 1, where surface-bound $^{\bullet}OH$ (TASP ($^{\bullet}OH$)) drives the initial hydroxylation of the polymer backbone, followed by chain scission and progressive oxidation. In addition, the fact that the degradation kinetics follow the pseudo-first-order model is consistent with a radical-dominated mechanism in which the concentration of reactive oxidants (e.g., $^{\bullet}OH$ and $SO_4^{\bullet-}$) is maintained quasi-steady by continuous electrogeneration, while the organic substrate concentration decays with time.

Moreover, FTIR results provide chemical-level confirmation of oxidative transformation of PS NPs and align strongly with Pathways 1 and 3. As shown in Figure 9b, the emergence of a distinct

carbonyl (C=O) band near ~1700 $cm^{-1}$ indicates the formation of oxygenated intermediates (ketones/aldehydes/carboxylic functionalities) during oxidation. Simultaneously, the pronounced reduction in aromatic C=C and C–H bands reflects degradation of the aromatic structure and loss of characteristic polystyrene features. This is consistent with oxidative attack on the phenyl-containing repeating units, formation of oxygenated aromatic intermediates (e.g., catechol/quinone-like species), and subsequent ring-opening and fragmentation. These spectral trends support not only surface $^{\bullet}OH$ oxidation but also indirect oxidation routes promoted by sulfate activation ($SO_4^{\bullet-}$ formation), as described in Pathway 3. Thus, the electrochemical signature, kinetic behavior, and chemical fingerprints collectively validate the proposed degradation framework and particularly emphasize the dominant contribution of radical-mediated oxidation.

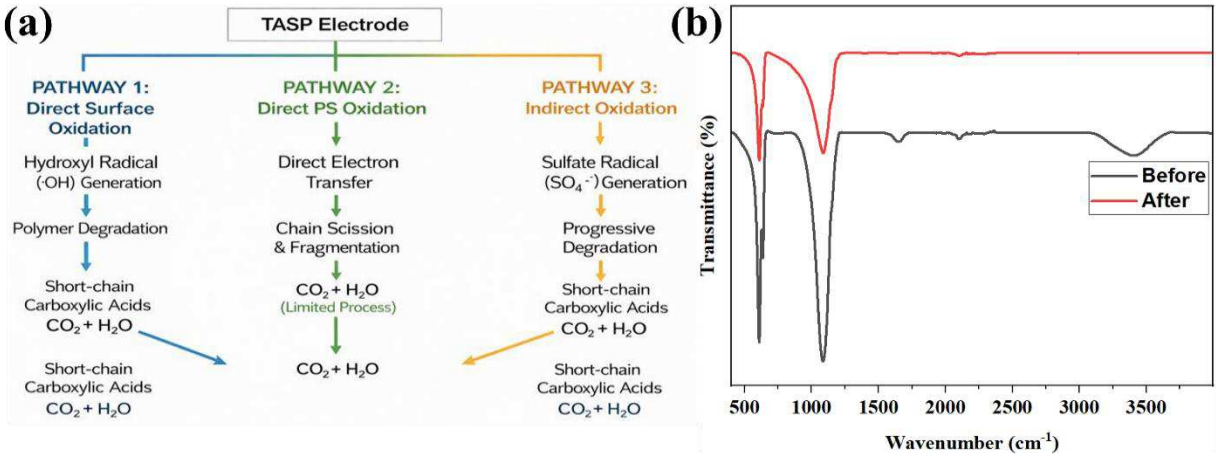



Figure 9. (a) Schematic mechanism of PS NPs degradation using TASP electrode; (b) FTIR spectra of PS NPs before and after EO process.

To experimentally probe the reactive species involved in PS-NP electro-oxidation, radical scavenging experiments were conducted under the optimized operating conditions, and the results are shown in Figure S5. In the absence of scavenger, removal efficiency reached 91.43%. Upon addition of tert-butanol (TBA), removal efficiency decreased to 61.2%, while addition of methanol (MeOH) further decreased it to 41.7%. The inhibition caused by TBA indicates that hydroxyl radicals ($^{\bullet}OH$) contribute significantly to PS-NP degradation. Moreover, the stronger suppression observed with MeOH suggests that sulfate radicals ($SO_4^{\bullet-}$) also play an important role, since MeOH scavenges both $^{\bullet}OH$ and $SO_4^{\bullet-}$, whereas TBA preferentially reacts with $^{\bullet}OH$. Therefore, the scavenging results support the proposed mechanism in which PS-NP degradation proceeds

mainly through a combined radical pathway involving both surface-generated $^{\bullet}OH$ and sulfate-derived radicals, while direct electron transfer is likely a secondary contribution.

### 3.8. TOC analysis of treated water

To further evaluate the extent of mineralization during PS-NP EO, total organic carbon (TOC) removal was measured under the optimized conditions, and the results are presented in Figure S6. TOC removal increased gradually with treatment time, reaching 43.1% at 90 min. In contrast, UV–Vis-based removal efficiency under the same optimized conditions reached 91.43% at 90 min. The lower TOC removal compared with UV–Vis removal indicates that disappearance of the characteristic PS absorbance does not correspond to complete mineralization. Instead, the EO process first promotes fragmentation of the polymer structure and loss of the original chromophoric/aromatic features, generating smaller dissolved intermediates that still contribute to solution TOC. With increasing electrolysis time, these intermediates undergo further oxidation, as reflected by the progressive increase in TOC removal. Therefore, the combined UV–Vis and TOC results suggest that PS NPs are efficiently degraded and partially mineralized during EO, while full mineralization is not achieved within the 90 min treatment period. This interpretation is also consistent with the proposed mechanism involving hydroxylation, chain scission, aromatic ring transformation, and subsequent oxidation of low-molecular-weight intermediates.

### 3.9. Comparison with previous electro-oxidation studies

To better position the present work within the existing literature, Table 4 compares representative Ti-based and $PbO_2$-based EO studies with the electrode and operating conditions used here. As shown, previous studies have mainly focused on dissolved pollutants such as chloramphenicol, ammonia, dye molecules, and phenolic compounds, while recent plastic-related work has more often targeted microplastics rather than PS NPs. In contrast, the present study specifically addresses PS NPs and employs the TASP multilayer anode under optimized conditions of pH 6.46, initial concentration 20 ppm, current density 11.44 mA $cm^{-2}$, and 90 min treatment time, achieving 91.43% experimental removal efficiency. In addition, unlike previous studies that typically examine electrode fabrication and degradation performance alone, the present work combines electrode synthesis with ANN-PSO modeling, GA optimization, and Garson-based sensitivity analysis. Notably, based on the literature surveyed, Ti/$PbO_2$, Ti/$TiO_2$/$PbO_2$, Ti/$TiO_2$-NTs/Sb-

737 $SnO_2/PbO_2$, and Ti/Ag/α-$PbO_2$/β-$PbO_2$ systems have been reported, but the exact TASP
738 configuration used here has not been identified. These distinctions support the novelty of the
739 present study from both material-design and process-analysis perspectives.
740
741 Table 4. Comparison of representative Ti-based and $PbO_2$-based EO studies with the present
742 work based on electrode structure and operating conditions.

| Study | Electrode | Pollutant | Concentration (ppm) | pH | Current density (mA $cm^{-2}$) | Time (min) | Removal rate (%) |
|---|---|---|---|---|---|---|---|
| This work | TASP | PS NPs | 20 | 6.46 | 11.44 | 90 | 91.43 |
| Liu et al. [17] | Ti/$PbO_2$-Co | Chloramphenicol | 10 | 5 | 15 | 50 | 99.9 |
| Zhang et al. [33] | $TiO_2$-NTs/Sb-$SnO_2/PbO_2$ | Ammonia nitrogen | 30 | 9 | 10 | 60 | 100 |
| He et al. [34] | Ti/$SnO_2$-$Sb_2O_4$-La/β-$PbO_2$ | Dye wastewater | 20 | 3 | 30 | 30 | 100 |
| Zhang et al. [77] | Ti/Cs-$SnO_2$/β-$PbO_2$ | Organic oxidation study | 30 | 3 | 30 | 60 | 90.9 |
| Ergu et al. [78] | Ti/Ag/α-$PbO_2$/β-$PbO_2$ | Alizarin red S | 40 | 5.5 | 40 | 180 | 98.8 |

743

744 **4. Conclusion**

745 In this study, a multilayer Ti/$TiO_2$–Ag–Sn/Pb–$PbO_2$ (TASP) anode was fabricated and applied for
746 the EO of PS NPs in water. The developed electrode exhibited improved electrochemical
747 characteristics compared with the reference systems, including a high oxygen-evolution potential
748 of 1.97 V vs Ag/AgCl, reduced charge-transfer resistance, and an extended accelerated service life
749 of 188 s under harsh test conditions. These results confirmed the beneficial effect of the Ag–Sn-
750 modified structure on activity and stability. Moreover, the effects of pH, initial PS-NP
751 concentration, and current density on removal efficiency were investigated using a maximin LHS
752 design augmented with a two-level factorial. Among the developed predictive tools, the ANN-PSO
753 model outperformed the quadratic RSM model, with higher accuracy ($R^2$ = 0.953; $R^2$_adj = 0.950)

and lower prediction error (RMSE = 2.125). This demonstrated its stronger ability to represent the nonlinear behavior of the EO process. Coupling ANN-PSO with the GA identified the optimum operating conditions as pH 6.46, initial concentration 20 ppm, and current density 11.44 mA $cm^{-2}$, with a predicted removal efficiency of 90.64%. Experimental validation under these conditions yielded 91.43% removal within 90 min, in excellent agreement with the model prediction. In addition, the degradation process followed pseudo-first-order kinetics, and the TASP electrode exhibited the highest apparent rate constant (0.0285 $min^{-1}$), approximately 3.2 times that of the unmodified TP electrode. Overall, this work demonstrates that combining an Ag–Sn-modified $PbO_2$-based anode with a data-driven modeling and optimization framework provides an effective and interpretable strategy for PS-NP removal.

**Declarations**

Consent to Publish declaration: Not applicable.

Consent to Participate declaration: Not applicable.

Author Contributions: S.M.E.Z. contributed to data curation, investigation, software (modelling), validation, formal analysis, and writing – original draft. M.F. contributed to investigation, modelling, methodology, supervision, project administration, and writing – review & editing. All authors reviewed and approved the manuscript.

Ethics declaration: Not applicable.

Competing Interests: The authors declare that they have no competing interests.

Funding: Not applicable.

Data availability: All data generated or analyzed during this study are included in this published article and its supplementary information files.

Safety and Environmental Considerations: All experiments were conducted in strict compliance with institutional safety guidelines. No hazardous materials or procedures were involved in this study. All experimental protocols were designed to minimize potential risks to researchers and the

environment. Data collection and analysis adhered to principles of accuracy, transparency, and reproducibility.

## References


1. Ali, I., et al., *Micro- and nanoplastics in wastewater treatment plants: Occurrence, removal, fate, impacts and remediation technologies – A critical review.* Chemical Engineering Journal, 2021. **423**: p. 130205.
2. Karimi Estahbanati, M.R., et al., *Treatment processes for microplastics and nanoplastics in waters: State-of-the-art review.* Marine Pollution Bulletin, 2021. **168**: p. 112374.
3. Feilizadeh, M., et al., *Combining nanofiltration and electrooxidation for complete removal of nanoplastics from water.* Marine Pollution Bulletin, 2025. **213**: p. 117621.
4. Kochaki, S.H., et al., *Conversion of waste micro/nano plastics into carbon materials: A new trend for renewable energy and environmental applications.* Applied Energy, 2026. **412**: p. 127690.
5. Lithner, D., Å. Larsson, and G. Dave, *Environmental and health hazard ranking and assessment of plastic polymers based on chemical composition.* Science of the total environment, 2011. **409**(18): p. 3309–3324.
6. Chatterjee, K. and T.K. Ghosh, *3D printing of textiles: potential roadmap to printing with fibers.* Advanced Materials, 2020. **32**(4): p. 1902086.
7. Kiendrebeogo, M., et al., *Nanoplastics removal from spiked laundry wastewater using electro-peroxidation process.* Chemosphere, 2023. **341**: p. 139963.
8. Karimi Estahbanati, M.R., et al., *Chapter 11 - Physical and physicochemical separation of microplastics and nanoplastics from water*, in *Current Developments in Biotechnology and Bioengineering*, R.D. Tyagi, et al., Editors. 2023, Elsevier. p. 269–292.
9. Feilizadeh, M., et al., *Chapter 13 - Chemical degradation of microplastics and nanoplastics in water and wastewater*, in *Current Developments in Biotechnology and Bioengineering*, R.D. Tyagi, et al., Editors. 2023, Elsevier. p. 315–332.
10. Hoang, N.T. and R. Holze, *Degradation of pesticide Cartap in Padan 95SP by combined advanced oxidation and electro-Fenton process.* Journal of solid state electrochemistry, 2021. **25**(1): p. 73–84.
11. Xu, L., et al., *Effective degradation of aqueous carbamazepine on a novel blue-colored TiO2 nanotube arrays membrane filter anode.* Journal of Hazardous Materials, 2021. **402**: p. 123530.
12. Nguyen Tien, H., et al., *Electrochemical degradation of indigo carmine, P-nitrosodimethylaniline and clothianidin on a fabricated Ti/$SnO_2$–Sb/Co-β$PbO_2$ electrode: Roles of radicals, water matrices effects and performance.* Chemosphere, 2023. **313**: p. 137352.
13. Groenen-Serrano, K., et al., *Role of Hydroxyl Radicals During the Competitive Electrooxidation of Organic Compounds on a Boron-Doped Diamond Anode.* Electrocatalysis, 2013. **4**(4): p. 346–352.
14. Feijoo, S., et al., *Generation of oxidative radicals by advanced oxidation processes (AOPs) in wastewater treatment: a mechanistic, environmental and economic review.* Reviews in Environmental Science and Bio/Technology, 2023. **22**(1): p. 205–248.

15. Hou, J., et al., *Electrochemical Oxidation of Methyl Orange in an Active Carbon Packed Electrode Reactor (ACPER): Degradation Performance and Kinetic Simulation.* International Journal of Environmental Research and Public Health, 2022. **19**(8): p. 4775.
16. Zhang, C., J. Liu, and B. Chen, *Effect of Ce(NO3)4 on the electrochemical properties of Ti/PbO2–TiO2–Ce(NO3)4 electrode for zinc electrowinning.* Applied Physics A, 2019. **125**(2): p. 150.
17. Liu, H., et al., *Ti/PbO2 electrode efficiency in catalytic chloramphenicol degradation and its effect on antibiotic resistance genes.* International Journal of Environmental Research and Public Health, 2022. **19**(23): p. 15632.
18. Liu, Y., et al., *A coupling mechanism of anodic oxygen evolution reaction during organic pollutants oxidation.* Journal of Electroanalytical Chemistry, 2023. **943**: p. 117608.
19. Molla, M.A.I., et al., *Optimization of Operating Conditions for Electrochemical Decolorization of Methylene Blue with Ti/α-$PbO_2$/β-$PbO_2$ Composite Electrode.* Journal of Composites Science, 2021. **5**(5): p. 117.
20. Du, L., J. Wu, and C. Hu, *Electrochemical oxidation of Rhodamine B on $RuO_2$–PdO–TiO2/Ti electrode.* Electrochimica Acta, 2012. **68**: p. 69–73.
21. Chen, S., et al., *Ag doping to boost the electrochemical performance and corrosion resistance of Ti/Sn–Sb-$RuO_x$/α-$PbO_2$/β-$PbO_2$ electrode in zinc electrowinning.* Journal of Alloys and Compounds, 2020. **815**: p. 152551.
22. Kawaguchi, K. and M. Morimitsu, *Reaction selectivity of IrO2-based nano/amorphous hybrid oxide-coated titanium anodes in acidic aqueous solutions: oxygen evolution and lead oxide deposition.* Journal of The Electrochemical Society, 2020. **167**(13): p. 133503.
23. Yan, Z., et al., *Promotion of in situ TiNx interlayer on morphology and electrochemical properties of titanium based $IrO_2$-$Ta_2O_5$ coated anode.* Journal of Alloys and Compounds, 2017. **708**: p. 1081–1088.
24. Dargahi, A., et al., *Parameter optimization and degradation mechanism for electrocatalytic degradation of 2,4-diclorophenoxyacetic acid (2,4-D) herbicide by lead dioxide electrodes.* RSC Advances, 2019. **9**(9): p. 5064–5075.
25. Tammam, R.H. and H. Hassan, *Enhancement of urea electrooxidation on $PbO_2$-Ni/C and Bi2O3-Ni/C nanocomposites in alkaline medium.* Journal of The Electrochemical Society, 2019. **166**(12): p. F729.
26. Hua, G., et al., *Fabrication and characterization of porous titanium-based $PbO_2$ electrode through the pulse electrodeposition method: Deposition condition optimization by orthogonal experiment.* Chemosphere, 2020. **261**: p. 128157.
27. Yao, Y., et al., *Electrochemical degradation of insecticide hexazinone with Bi-doped $PbO_2$ electrode: Influencing factors, intermediates and degradation mechanism.* Chemosphere, 2019. **216**: p. 812–822.
28. Kong, J., et al., *Preparation and characterization of $PbO_2$ electrodes doped with different rare earth oxides.* Electrochimica Acta, 2007. **53**(4): p. 2048–2054.
29. Chen, Z., et al., *A novel Pb/$PbO_2$ electrodes prepared by the method of thermal oxidation-electrochemical oxidation: Characteristic and electrocatalytic oxidation performance.* Journal of Alloys and Compounds, 2021. **851**: p. 156834.
30. Zhou, S., et al., *Study on electrochemical properties of active coating PbO2-CeO2 reinforced Al-based composite coating electrode.* Journal of Materials Science: Materials in Electronics, 2022. **33**(21): p. 17223–17234.
31. Ho, N.A.D., et al., *SnO2-Mixed Oxide Electrodes for Water Treatment: Role of the Low-*

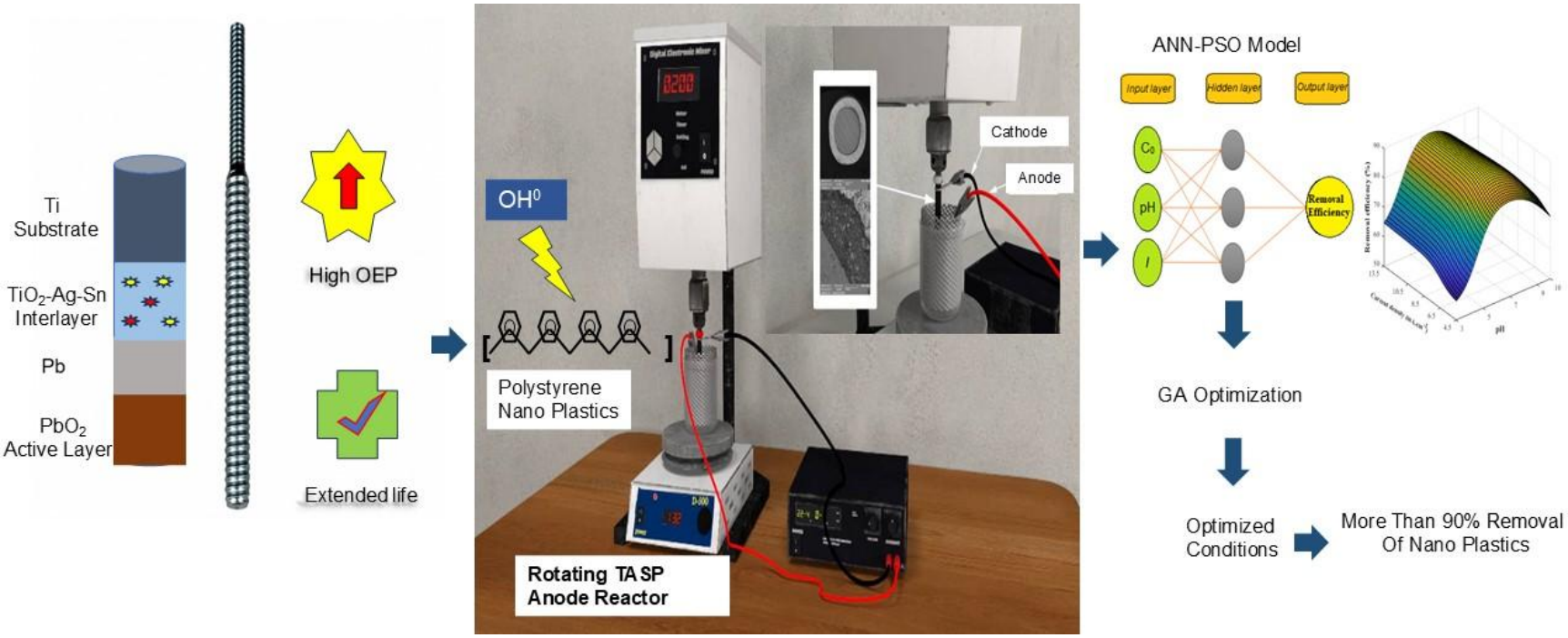
*Cost Active Anode*, in *Cost-efficient Wastewater Treatment Technologies: Engineered Systems*, M. Nasr and A.M. Negm, Editors. 2023, Springer International Publishing: Cham. p. 255–284.
32. Benvidi, A., et al., *Fabrication of several $SnO_2$-based anodes for electrochemical ozone generation: comparison, characterization and application.* Research on Chemical Intermediates, 2021. **47**(11): p. 4803–4824.
33. Zhang, Z., et al., *Construction of the multi-layer $TiO_2$-NTs/Sb-$SnO_2$/$PbO_2$ electrode for the highly efficient and selective oxidation of ammonia in aqueous solution: Characterization, performance and mechanism.* Journal of Environmental Chemical Engineering, 2023. **11**(3): p. 109834.
34. He, Y., et al., *Preparation of Ti/SnO2-Sb2O4-La/β-PbO2 electrode and its electrochemical oxidation performance of dye wastewater.* Microchemical Journal, 2024. **205**: p. 111378.
35. Guo, J., et al., *Preparation of Ti/Sn-$SbO_x$/β-$PbO_2$-$Ta_2O_5$ composite anode by pulsed electrodeposition and its electrochemical properties.* Solid State Ionics, 2024. **408**: p. 116477.
36. Nguyen Tien, H. and F.M. Mwazighe, *Preparation of Ti/$SnO_2$–Sb/La-β$PbO_2$ electrode and its application in the degradation of some pollutants including prednisolone and 8-Hydroxyquinoline.* Chemosphere, 2023. **333**: p. 138933.
37. Liu, Z., et al., *Electrocatalytic oxidation of gaseous toluene in an all-solid cell using a foam Ti/Sb-$SnO_2$/β-$PbO_2$ anode.* Journal of Environmental Sciences, 2023. **134**: p. 77–85.
38. Homaeigohar, S., R. Kabir, and M. Elbahri, *Size-Tailored Physicochemical Properties of Monodisperse Polystyrene Nanoparticles and the Nanocomposites Made Thereof.* Scientific Reports, 2020. **10**(1): p. 5191.
39. Jung, M.-H., et al., *ZnO nanosphere fabrication using the functionalized polystyrene nanoparticles for dye-sensitized solar cells.* Electrochimica acta, 2010. **55**(22): p. 6563–6569.
40. Nuruzatulifah, A., A. Nizam, and N.N. Ain, *Synthesis and characterization of polystyrene nanoparticles with covalently attached fluorescent dye.* Materials Today: Proceedings, 2016. **3**: p. S112–S119.
41. Morris, M.D. and T.J. Mitchell, *Exploratory designs for computational experiments.* Journal of statistical planning and inference, 1995. **43**(3): p. 381–402.
42. Estahbanati, M.K., M. Feilizadeh, and M.C. Iliuta, *Photocatalytic valorization of glycerol to hydrogen: Optimization of operating parameters by artificial neural network.* Applied Catalysis B: Environmental, 2017. **209**: p. 483–492.
43. Feilizadeh, M., et al., *Individual and interaction effects of operating parameters on the photocatalytic degradation under visible light illumination: Response surface methodological approach.* The Canadian Journal of Chemical Engineering, 2017. **95**(7): p. 1228–1235.
44. Bararpour, S.T., et al., *Investigation of 2-nitrophenol solar degradation in the simultaneous presence of $K_2S_2O_8$ and $H_2O_2$: using experimental design and artificial neural network.* Journal of cleaner production, 2018. **176**: p. 1154–1162.
45. Rajabi, S., et al., *Synergistic degradation of metronidazole and penicillin G in aqueous solutions using $AgZnFe_2O_4$@chitosan nano-photocatalyst under UV/persulfate activation.* Environmental Technology & Innovation, 2024. **35**: p. 103724.
46. Pizarroso, J., J. Portela, and A. Muñoz, *NeuralSens: sensitivity analysis of neural networks.* arXiv preprint arXiv:2002.11423, 2020.

47. Bolton, J.R., et al., *Figures-of-merit for the technical development and application of advanced oxidation technologies for both electric-and solar-driven systems (IUPAC Technical Report).* Pure and Applied Chemistry, 2001. **73**(4): p. 627–637.
48. Vardhan, P.V. and L.I. Shukla, *FT-IR investigations on effect of high doses of gamma radiation-induced damage to polystyrene and mechanism of formation of radiolysis products.* Radiation and Environmental Biophysics, 2018. **57**: p. 301–310.
49. Elaissaoui, I., H. Akrout, and L. Bousselmi, *Interface behavior of PbO2 on pure lead and stainless steel as anode for dye degradation.* Desalination and Water Treatment, 2016. **57**(34): p. 16161–16176.
50. Toro, R.G., et al., *Study of the effect of titanium dioxide hydrosol on the photocatalytic and mechanical properties of paper sheets.* Materials, 2020. **13**(6): p. 1326.
51. Fatemeh, K., M. Mohammad Javad, and K. Samaneh, *The effect of silver nanoparticles on composite shear bond strength to dentin with different adhesion protocols.* Journal of applied oral science, 2017. **25**: p. 367–373.
52. Arora, N. and B.R. Jagirdar, *From (Au 5 Sn+ AuSn) physical mixture to phase pure AuSn and Au 5 Sn intermetallic nanocrystals with tailored morphology: digestive ripening assisted approach.* Physical Chemistry Chemical Physics, 2014. **16**(23): p. 11381–11389.
53. Tot, P.T., M.T.T. Thuy, and P.T. Binh, *Electrochemical characterization of $PbO_2$-$TiO_2$ composite prepared on stainless steel substrate by cyclic voltammetry method.* Vietnam Journal of Science and Technology, 2022. **60**(4): p. 631640–631640.
54. Wang, Q., et al., *Optimized Indium modified Ti/PbO2 anode for electrochemical degradation of antibiotic cefalexin in aqueous solutions.* Colloids and Surfaces A: Physicochemical and Engineering Aspects, 2021. **628**: p. 127244.
55. Wang, S., et al., *Regulating the concentration of dissolved oxygen to achieve the directional transformation of reactive oxygen species: A controllable oxidation process for ciprofloxacin degradation by calcined CuCoFe-LDH.* Water Research, 2023. **233**: p. 119744.
56. Meng, Y., et al., *Structure–property relationship of bifunctional $MnO_2$ nanostructures: highly efficient, ultra-stable electrochemical water oxidation and oxygen reduction reaction catalysts identified in alkaline media.* Journal of the American Chemical Society, 2014. **136**(32): p. 11452–11464.
57. Li, C., et al., *Novel strategy for the efficient degradation of organic contaminants using porous graphite electrodes: Synergistic mechanism of anodic and cathodic reactions.* Chemical Engineering Journal, 2022. **429**: p. 132340.
58. Chaharmahali, R., et al., *A systematic study on modulation of plasma electrolytic oxidation parameters for optimizing photocatalytic coatings on titanium substrates.* Journal of Alloys and Compounds, 2023. **963**: p. 171234.
59. Su, Y.-f., et al., *Photoelectrocatalytic degradation of the antibiotic sulfamethoxazole using TiO2/Ti photoanode.* Applied Catalysis B: Environmental, 2016. **186**: p. 184–192.
60. Li, X., H. Xu, and W. Yan, *Preparation and characterization of PbO 2 electrodes modified with polyvinyl alcohol (PVA).* Rsc Advances, 2016. **6**(85): p. 82024–82032.
61. Xu, L., Y. Wang, and W. Zhang, *Preparation of a SnO 2–Sb electrode on a novel TiO 2 network structure with long service lifetime for degradation of dye wastewater.* RSC advances, 2019. **9**(67): p. 39242–39251.
62. Moradi, S., et al., *Photocatalytic degradation of dibenzothiophene using La/PEG-modified TiO2 under visible light irradiation.* Research on Chemical Intermediates, 2015. **41**(7): p.

4151–4167.
63. Periyasamy, S. and M. Muthuchamy, *Electrochemical oxidation of paracetamol in water by graphite anode: Effect of pH, electrolyte concentration and current density.* Journal of Environmental Chemical Engineering, 2018. **6**(6): p. 7358–7367.
64. Bouya, H., et al., *Electrochemical Oxidation of 2-Nitrobenzaldehyde on Boron-Doped Diamond Anodes.* International Journal of Electrochemical Science, 2013. **8**(5): p. 7468–7478.
65. Li, Y., et al., *Anodic oxidation using 3D carbon felt/$PbO_2$ anode: a electron transfer-mediated system for degradation of Rhodamine B.* Environmental Technology, 2025. **46**(16): p. 3047–3064.
66. Chun, M.-S., H.I. Cho, and I.K. Song, *Electrokinetic behavior of membrane zeta potential during the filtration of colloidal suspensions.* Desalination, 2002. **148**(1-3): p. 363–368.
67. Zheng, W., et al., *Effective degradation of polystyrene microplastics by Ti/La/Co-Sb-$SnO_2$ anodes: Enhanced electrocatalytic stability and electrode lifespan.* Science of The Total Environment, 2024. **922**: p. 171002.
68. Dong, H., et al., *Co/La modified Ti/$PbO_2$ anodes for chloramphenicol degradation: Catalytic performance and reaction mechanism.* Chemosphere, 2021. **285**: p. 131568.
69. Hoang, N.T., et al., *Kinetic study on methylene blue removal from aqueous solution using UV/chlorine process and its combination with other advanced oxidation processes.* Chemosphere, 2022. **308**: p. 136457.
70. Noudeh, G.D., et al., *Response surface modeling of ceftriaxone removal from hospital wastewater.* Environmental Monitoring and Assessment, 2023. **195**(1): p. 217.
71. Chen, Y.-L., et al., *Electrocatalytic hydrodehalogenation of atrazine in aqueous solution by Cu@Pd/Ti catalyst.* Chemosphere, 2015. **125**: p. 57–63.
72. Zhang, Y., et al., *Ti/$PbO_2$-$Sm_2O_3$ composite based electrode for highly efficient electrocatalytic degradation of alizarin yellow R.* Journal of colloid and interface science, 2019. **533**: p. 750–761.
73. Jarvis, P. and J. Fawell, *Lead in drinking water – An ongoing public health concern?* Current Opinion in Environmental Science & Health, 2021. **20**: p. 100239.
74. Comninellis, C., *Electrocatalysis in the electrochemical conversion/combustion of organic pollutants for waste water treatment.* Electrochimica acta, 1994. **39**(11-12): p. 1857–1862.
75. Panizza, M. and G. Cerisola, *Direct and mediated anodic oxidation of organic pollutants.* Chemical reviews, 2009. **109**(12): p. 6541–6569.
76. Martinez-Huitle, C.A. and S. Ferro, *Electrochemical oxidation of organic pollutants for the wastewater treatment: direct and indirect processes.* Chemical society reviews, 2006. **35**(12): p. 1324–1340.
77. Zhang, R., et al., *Strategy for enhancing the electrocatalytic performance of Ti/β-PbO2 anode: Optimizing SnO2 intermediate layer by Cs doping and application for the efficient removal of mixed fluoroquinolones.* Journal of Alloys and Compounds, 2022. **895**: p. 162528.
78. Ergu, A., J. Yu, and X. Jiang, *Interfacial engineering via silver mirror reaction: Boosting electrocatalytic activity and stability of the Ti/PbO2 electrode.* Separation and Purification Technology, 2025. **377**: p. 134379.

1006

## Graphical Abstract




1007

## Supplementary Files

This is a list of supplementary files associated with this preprint. Click to download.

- Supplementaryinformation3Graphical.docx
- highlights2.docx